Molecular Cell

Article

Spatial control of m^{6}A deposition on enhancer and promoter RNAs through co-acetylation of METTL3 and H3K27 on chromatin

Graphical abstract

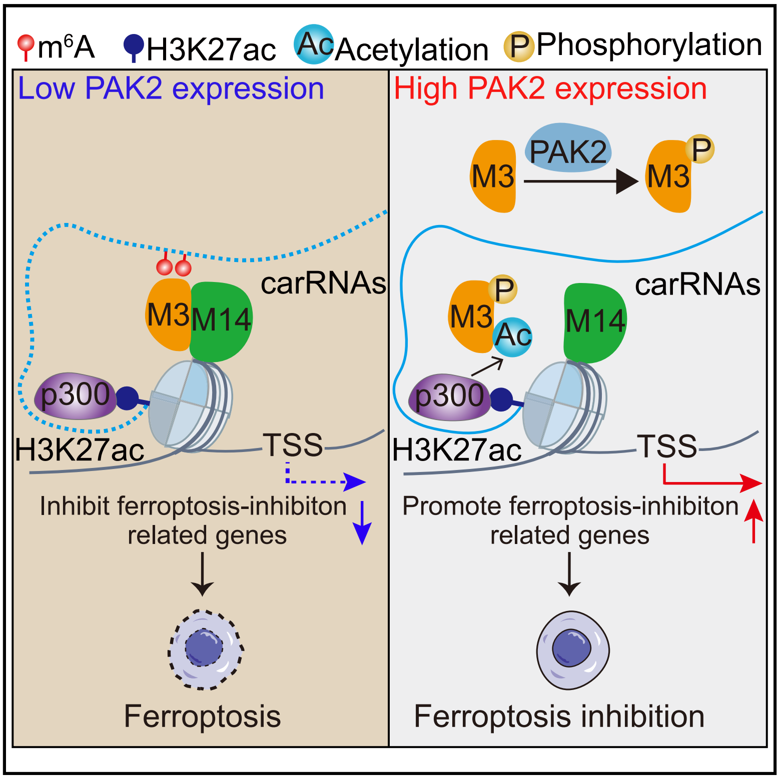

Highlights

- p300 acetylates METTL3 specifically on H3K27ac chromatin
- Acetylated METTL3 disassociates from H3K27ac through impaired binding with METTL14
- METTL3 acetylation selectively inhibits m^{6}A of eRNAs and paRNAs
- PAK2 promotes METTL3 acetylation by phosphorylating METTL3 to inhibit ferroptosis

Authors

Xiang Huang, Jie Zhang, Yixian Cun, ..., Zehong Wu, Xiaofeng Zhu, Jinkai Wang

Correspondence

wangjk@mail.sysu.edu.cn

In brief

Huang et al. find that H3K27ac acetylase p300 mainly acetylates METTL3 on H3K27ac-marked chromatin, resulting in specific m^{6}A inhibition of enhancer and promoter RNAs through METTL14-mediated disassociation from H3K27ac. PAK2 promotes METTL3 acetylation by phosphorylating METTL3 to inhibit ferroptosis and promote cancer cell survival. This study reveals a spatial-selective way of regulating m^{6}A.

Huang et al., 2025, Molecular Cell *85*, 1–17
April 3, 2025
https://doi.org/10.1016/j.molcel.2025.02.016

Please cite this article in press as: Huang et al., Spatial control of m^{6}A deposition on enhancer and promoter RNAs through co-acetylation of METTL3 and H3K27 on chromatin, Molecular Cell (2025), https://doi.org/10.1016/j.molcel.2025.02.016

Molecular Cell

CellPress

Article

Spatial control of m^{6}A deposition on enhancer and promoter RNAs through co-acetylation of METTL3 and H3K27 on chromatin

Xiang Huang,[1,2,3,6] Jie Zhang,[1,2,6] Yixian Cun,[1,2,6] Meijun Ye,[1,2,6] Zhijun Ren,[1,2,3,6] Wenbing Guo,[1,2,3] Xiaojun Ma,[1,2] Jiayin Liu,[1,2] Weiwei Luo,[4] Xiang Sun,[1,2] Jingwen Shao,[1,2] Zehong Wu,[1,2] Xiaofeng Zhu,[5] and Jinkai Wang[1,2,7,*]

[1]Department of Histoembryology and Cell Biology, Zhongshan School of Medicine, Sun Yat-sen University, Guangzhou 510080, China

[2]Center for Stem Cell Biology and Tissue Engineering, Key Laboratory for Stem Cells and Tissue Engineering, Ministry of Education, Sun Yat-sen University, Guangzhou 510080, China

[3]Medical College of Jiaying University, Meizhou 514031, China

[4]GeneMind Biosciences Company Limited, Shenzhen 518000, China

[5]State Key Laboratory of Oncology in South China, Collaborative Innovation Center for Cancer Medicine, Sun Yat-sen University Cancer Center, Guangzhou 518000, China

[6]These authors contributed equally

[7]Lead contact

*Correspondence: wangjk@mail.sysu.edu.cn

https://doi.org/10.1016/j.molcel.2025.02.016

SUMMARY

Interaction between the N^6-methyladenosine (m^{6}A) methyltransferase METTL3 and METTL14 is critical for METTL3 to deposit m^{6}A on various types of RNAs. It remains to be uncovered whether there is spatial control of m^{6}A deposition on different types of RNAs. Here, through genome-wide CRISPR-Cas9 screening in the A549 cell line, we find that H3K27ac acetylase p300-mediated METTL3 acetylation suppresses the binding of METTL3 on H3K27ac-marked chromatin by inhibiting its interaction with METTL14. Consistently, p300 catalyzing the acetylation of METTL3 specifically occurs on H3K27ac-marked chromatin. Disruptive mutations on METTL3 acetylation sites selectively promote the m^{6}A of chromatin-associated RNAs from p300-bound enhancers and promoters marked by H3K27ac, resulting in transcription inhibition of ferroptosis-inhibition-related genes. In addition, PAK2 promotes METTL3 acetylation by phosphorylating METTL3. Inhibition of PAK2 promotes ferroptosis in a manner that depends on the acetylation of METTL3. Our study reveals a spatial-selective way to specifically regulate the deposition of m^{6}A on enhancer and promoter RNAs.

INTRODUCTION

In mammalian cells, N^6-methyladenosine (m^{6}A) is an abundant and reversible RNA modification on diverse types of RNAs.[1,2] It has been revealed that they play important roles in various physiological and pathological processes by regulating the transcriptional as well as posttranscriptional processes of RNAs.[3–7] The m^{6}A is mainly catalyzed by a multicomponent methyltransferase complex (MTC), consisting of METTL3, METTL14, WTAP (Wilms' tumor 1-associating protein), VIRMA, ZC3H13, HAKAI (also known as CBLL1), and RBM15/15B.[8–12] METTL3/METTL14 heterodimer is the catalytic subunit in the m^{6}A writer complex, in which only METTL3 has catalytic activity and METTL14 is critical for binding of METTL3 on RNAs.[13] Thus, the interaction of METTL3 with METTL14 is critical for METTL3 to catalyze m^{6}A deposition on RNAs. However, whether and how the interaction between METTL3 and METTL14 could be dynamically and specifically regulated to modulate the m^{6}A on specific RNAs is largely unknown.

m^{6}A can be deposited on RNAs both co-transcriptionally and post-transcriptionally after splicing.[14–19] Histone modifications could also regulate the deposition of m^{6}A on chromatin RNAs. It was reported that histone modification H3K36me3, which is related to transcription elongation, can facilitate the m^{6}A on gene bodies by recruiting METTL3 to the chromatin through interaction with METTL14.[20] On the other hand, the chromatin-associated regulatory RNAs (carRNAs), mainly composed of repeat RNAs, enhancer RNAs (eRNAs), and promoter-associated non-coding RNAs (paRNAs), were also found to be m^{6}A methylated; the m^{6}A of carRNAs facilitates the degradation of these regulatory RNAs for the transcriptional inhibition of the downstream targeted genes.[2] Further studies revealed that the localization of the core MTC components are enriched in the chromatin regions marked by H3K27ac to facilitate the m^{6}A methylation of eRNAs and paRNAs for transcription activation.[21,22] Recent studies revealed that regulating the m^{6}A on eRNAs and paRNAs is crucial for tumorigenesis.[23,24]

Regulation of the m^{6}A on RNAs relies on the protein interactions with MTC, protein posttranslational modifications also

Please cite this article in press as: Huang et al., Spatial control of m^{6}A deposition on enhancer and promoter RNAs through co-acetylation of METTL3 and H3K27 on chromatin, Molecular Cell (2025), https://doi.org/10.1016/j.molcel.2025.02.016

play important roles in regulating the protein-protein interactions in diverse biological processes.[25] Indeed, different types of modifications of the components of MTC have been reported to play regulatory roles on m^{6}A, including phosphorylation of METTL3 and WTAP,[26,27] SUMOylation (small ubiquitin-like modifier modification) of METTL3,[28] and arginine methylation of METTL14.[29] Recently, acetylation of METTL3 in the cytoplasm was reported to regulate translation.[30,31] However, whether posttranslational modifications of MTC components regulate the assembly of MTC is still unknown. Here, in contrast to the previous studies, we find that the H3K27ac acetylase p300 mainly acetylates METTL3 on H3K27ac-marked chromatin and further reveals a mechanism for spatial-specific regulation of m^{6}A.

RESULTS

Identification of p300 and PAK2 as negative regulators of METTL3 interacting with METTL14

To screen for the genes that regulate the interaction between METTL3 and METTL14, we construct a bimolecular fluorescence complementation (BIFC)-system-based reporter,[32] which indicates the binding intensity of METTL3 with METTL14 by bringing together the two complementary non-fluorescent fragments (Figure 1A). Subsequently, we established a stable A549 cell line containing the TETon (tetracycline-controlled transcriptional activation system)-BIFC reporter (Figure S1A). As expected, we found that METTL3 or METTL14 knockdown significantly decreased the yellow fluorescence of the TETon-BIFC reporter in A549 cells (Figure S1B).

We then transduced A549 cells stably expressing the TETon-BIFC reporter with the lentiviral library of CRISPR-Cas9 sgRNAs (single guide RNAs) (targeting 19,114 genes) to perform whole-genome screening for genes regulating the interaction between METTL3 and METTL14[33] (Figure 1B). After activating the expression of TETon-BIFC reporter using doxycycline for 48 h, we sorted the cells with the top and bottom 5% of yellow fluorescence intensity by fluorescence-activated cell sorting (FACS), followed by high-throughput sequencing of the amplified sgRNAs (Figure S1C). We found that the sgRNAs of 985 and 817 genes were significantly enriched in the cells with high and low fluorescence intensities (Table S1). As expected, the sgRNAs of METTL3 were dramatically enriched in cells with low fluorescence intensities (Figure S1D). Interestingly, GO (Gene Ontology) enrichment analysis revealed that the genes with sgRNA significantly overrepresented in the cell with high fluorescence intensities were significantly enriched in the terms involved in the histone acetyltransferase complex and protein kinase complex, which is consistent with the previous studies that acetylation and phosphorylation play critical roles in the regulation of protein-protein interaction[34,35] (Figure 1C). Thus, these acetyltransferase complex and protein kinase complex-associated genes might regulate the interaction of METTL3 with METTL14 by mediating METTL3 post-translation modifications. Subsequently, we tested the sgRNA of *EP300* (Figure 1D), which encodes the H3K27ac acetylase p300, because it emerged as one of the most enriched genes from the histone acetyltransferase complex in our screening. In addition, since METTL3/METTL14 heterodimer mainly localizes on nuclear to facilitate m^{6}A deposition, we also tested the genes encoding nuclear- or chromatin-localized proteins from the protein kinase complex, including *PAK2*, *CDK2*, *CDK13*, and *CAMK2G* (Figure 1D). First of all, based on the overrepresented sgRNAs, we confirmed that knockout of these genes dramatically enhanced the fluorescence intensity of TETon BIFC reporter, respectively (Figures S1E and S1F). We hereby focused on *EP300* and *PAK2*, a serine/threonine protein kinase highly expressed in various cancers,[36] because their sgRNAs had the most significant effects on the fluorescence of TETon BIFC reporter. Collectively, p300 and PAK2 are potential inhibitors of METTL3 interacting with METTL14, which might be dependent on the acetylation and phosphorylation of METTL3.

p300 acetylates METTL3 on H3K27ac-bound chromatin

p300 protein is a well-characterized transcription co-activator and mainly localizes on chromatin responsible for H3K27ac formation.[37,38] A previous study reported that p300 acetylates METTL3 in the cytoplasm to inhibit the nuclear translocation of METTL3.[30] We confirmed that the acetylation level of FLAG-tagged METTL3 was dramatically increased after treating HEK293T cells with the mixture of the inhibitors of two classes of cellular deacetylase, including nicotinamide (NAM), an inhibitor of the SIRT (sirtuin) family deacetylases, and trichostatin A (TSA), an inhibitor of histone deacetylase (HDAC) classes I, II, and IV (Figure 2A), indicating that cellular METTL3 is acetylated. Because p300 can localize in both nuclear and cytoplasm, we tested whether p300 can promote the METTL3 acetylation in nuclear and cytoplasm cell fractions, respectively. In contrast to the previous study, we found that p300 overexpression promotes the acetylation of FLAG-tagged METTL3 in both nuclear and cytoplasm. Since p300 is mainly localized in nuclear, the p300-induced METTL3 acetylation was much more dominant in nuclear than the cytoplasm (Figure 2B). Immunofluorescence analysis also confirmed that p300 mainly co-localizes with METTL3 in nuclear (Figure 2C). These results suggest that p300 may play a more important role in acetylating the nuclear-localized METTL3 than cytoplasmic METTL3.

Since p300 is the acetylase of H3K27ac, which is the marker of open chromatin and active enhancers and promoters, we therefore tested whether p300 acetylates both METTL3 and H3K27ac on chromatin. Interestingly, we found that METTL3 simultaneously co-localizes with p300 and H3K27ac in the nuclear using immunofluorescence (Figure S2A). Spatial co-localization of METTL3, H3K27ac, and p300 was also observed using three-dimensional structured illumination microscopy 3D-SIM (3D structured illumination microscopy) (Figure 2D). Based on microscopy image analysis,[39] we found 71.8% of p300-bound METTL3 simultaneously co-localized with H3K27ac (Figure 2E). Consistently, through isolating the cytoplasm, nucleoplasm, and chromatin fractions of the HEK293T cells (Figures S2B and S2C), we found that the vast majority of acetylated METTL3 were in chromatin fractions other than cytoplasm or nucleoplasm fractions (Figure 2F). We further found that p300 knockdown mainly decreased the acetylation of METTL3 in the isolated chromatin of HEK293T cells (Figure 2G). Consistently, overexpression of p300 significantly increases the acetylation

Please cite this article in press as: Huang et al., Spatial control of m^{6}A deposition on enhancer and promoter RNAs through co-acetylation of METTL3 and H3K27 on chromatin, Molecular Cell (2025), https://doi.org/10.1016/j.molcel.2025.02.016

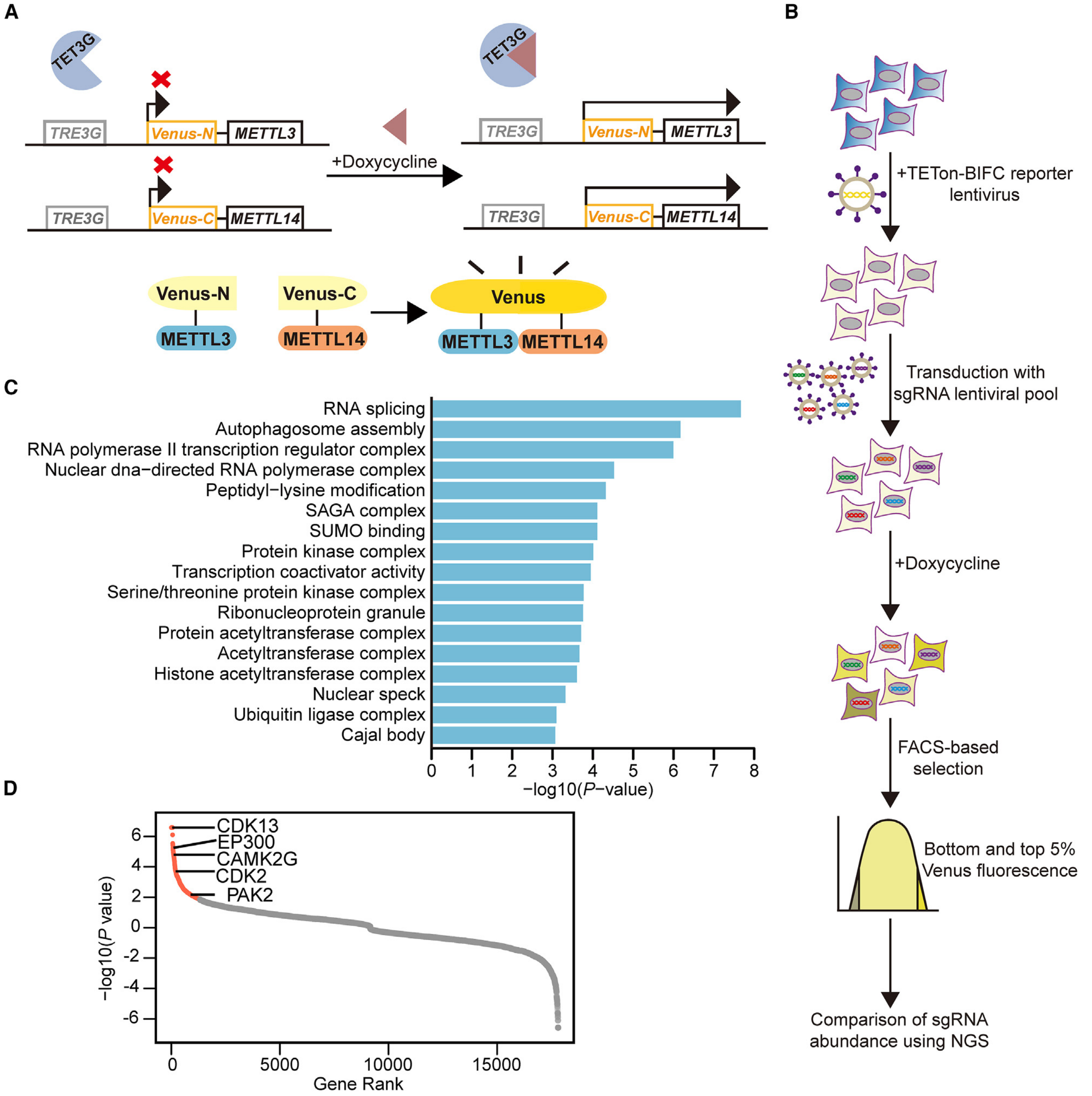

Figure 1. p300 and PAK2 are negative regulators of interaction between METTL3 with METTL14

(A) Schematic diagram of TETon-BIFC reporter.

(B) Overview of the CRISPR screen.

(C) GO enrichment analysis of genes with sgRNA significantly overrepresented in the cells with high fluorescence intensities. *p* values were calculated by one-sided hypergeometric test.

(D) Ranked *p* values of the sgRNAs in genome-wide CRISPR-Cas9 screening. The representative genes were indicated.

See also Figure S1 and Table S1.

of chromatin-associated FLAG-tagged METTL3, as well as the acetylation of endogenous chromatin-associated METTL3 (Figures 2H and S2D). Similar results were also observed in A549 cells (Figures S2E–S2H). These results indicate that p300 acetylates METTL3 mainly on H3K27ac-bound chromatin.

Three acetylation sites of METTL3 are acetylated by p300 on chromatin

To identify acetylation sites of chromatin-associated METTL3, FLAG-tagged METTL3 was isolated by chromatin fraction extraction combined with co-immunoprecipitation (coIP) from

Please cite this article in press as: Huang et al., Spatial control of m^{6}A deposition on enhancer and promoter RNAs through co-acetylation of METTL3 and H3K27 on chromatin, Molecular Cell (2025), https://doi.org/10.1016/j.molcel.2025.02.016

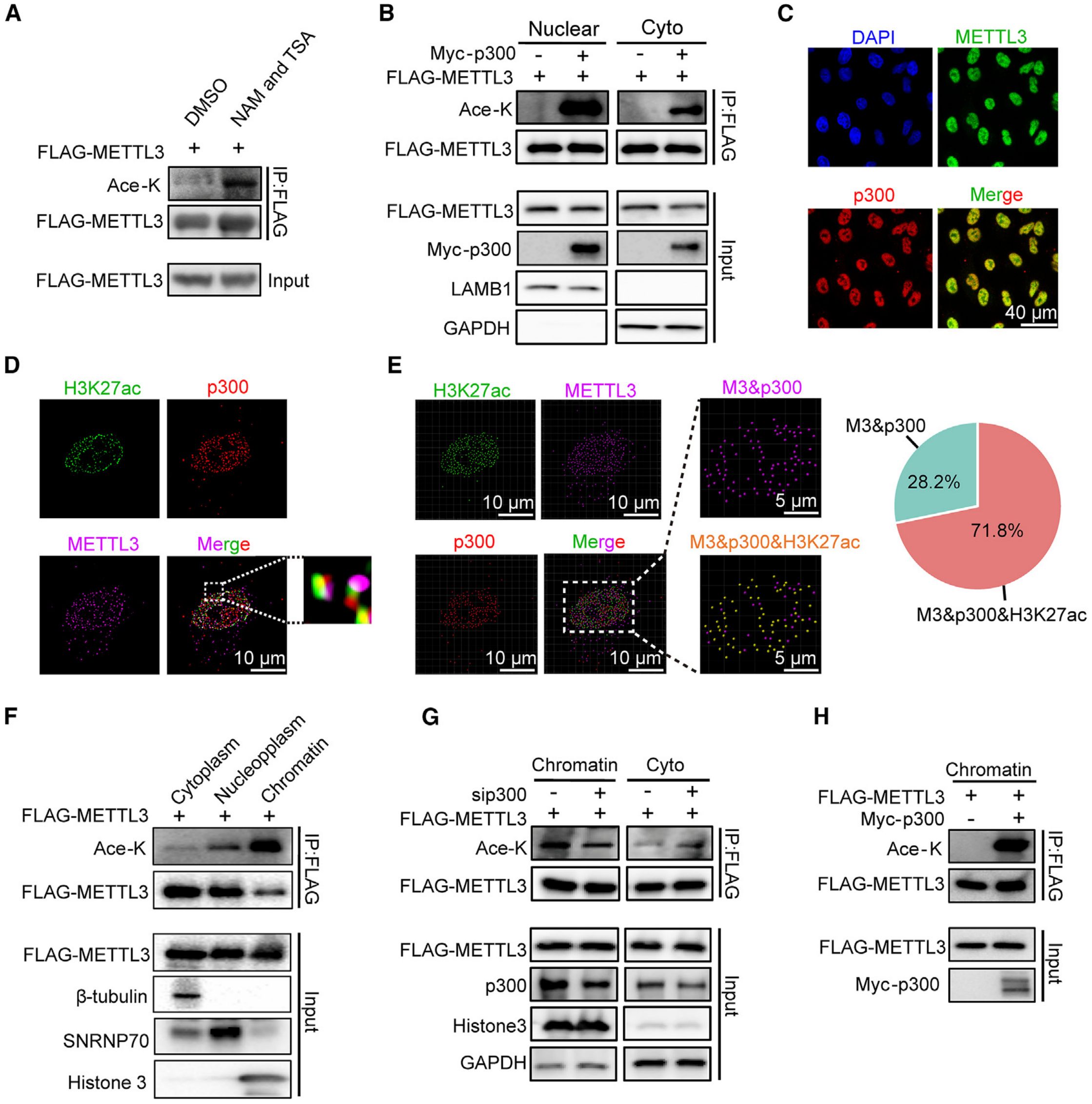

Figure 2. p300 acetylates METTL3 on H3K27ac-bound chromatin

(A) CoIP detects METTL3 acetylation following treatment with deacetylase inhibitors TSA (1 μM) and NAM (5 mM) for 6 h in HEK293T cells.

(B) CoIP was used to detect the METTL3 acetylation in the nuclear and cytoplasmic lysates of HEK293T cells transfected as indicated.

(C) Immunofluorescence analysis of DAPI (blue), METTL3 (green), and p300 (red) in HEK293T cells. Scale bars: 40 μm.

(D) 3D-SIM illuminated localization of METTL3 (purple), p300 (red), and H3K27ac (green) in HEK293T cells. Scale bars, 10 μm.

(E) The spot model of Imaris software was used to reconstruct METTL3, p300, and H3K27ac based on 3D-SIM data (left), which was used to calculate their co-localization relationship. The fractions of METTL3 proteins colocalize with both p300 and H3K27ac (M3 & p300 & H3K27ac), as well as the METTL3 proteins only colocalize with p300 but not H3K27ac (M3 & p300), are depicted in the pie chart (right).

(F) CoIP was used to detect the METTL3 acetylation in the cytoplasm, soluble nuclear, and chromatin lysates of HEK293T cells transfected as indicated.

(G) Chromatinic and cytoplasmic lysates of HEK293T cells, transfected as indicated, were analyzed by coIP to detect METTL3 acetylation.

(H) Chromatinic lysates of HEK293T cells, transfected as indicated, were analyzed by coIP to detect METTL3 acetylation.

See also Figure S2.

p300 overexpressed and control HEK293T cells and then analyzed by mass spectrometry. Of five high confidences p300-dependent lysine acetylation sites in chromatin-associated METTL3, K177, K211, K215, K327, and K578 were detected (Figures 3A and S3A–S3C). Protein sequence alignment[40] of METTL3 homologs from representative vertebrates showed that all these five lysine acetylation sites are evolutionarily conserved in mammals (Figure S3D). Consistent with mass spectrometry, we truncated METTL3 and found that the acetylation exists in 1–350 and 351–580 amino acids of chromatin-associated METTL3, respectively (Figure S3E). To validate whether these lysine acetylation sites of METTL3 are target sites of p300, we mutated each lysine K to arginine R to mimic acetylation-inactivation to detect the change of chromatin-associated

Please cite this article in press as: Huang et al., Spatial control of m^{6}A deposition on enhancer and promoter RNAs through co-acetylation of METTL3 and H3K27 on chromatin, Molecular Cell (2025), https://doi.org/10.1016/j.molcel.2025.02.016

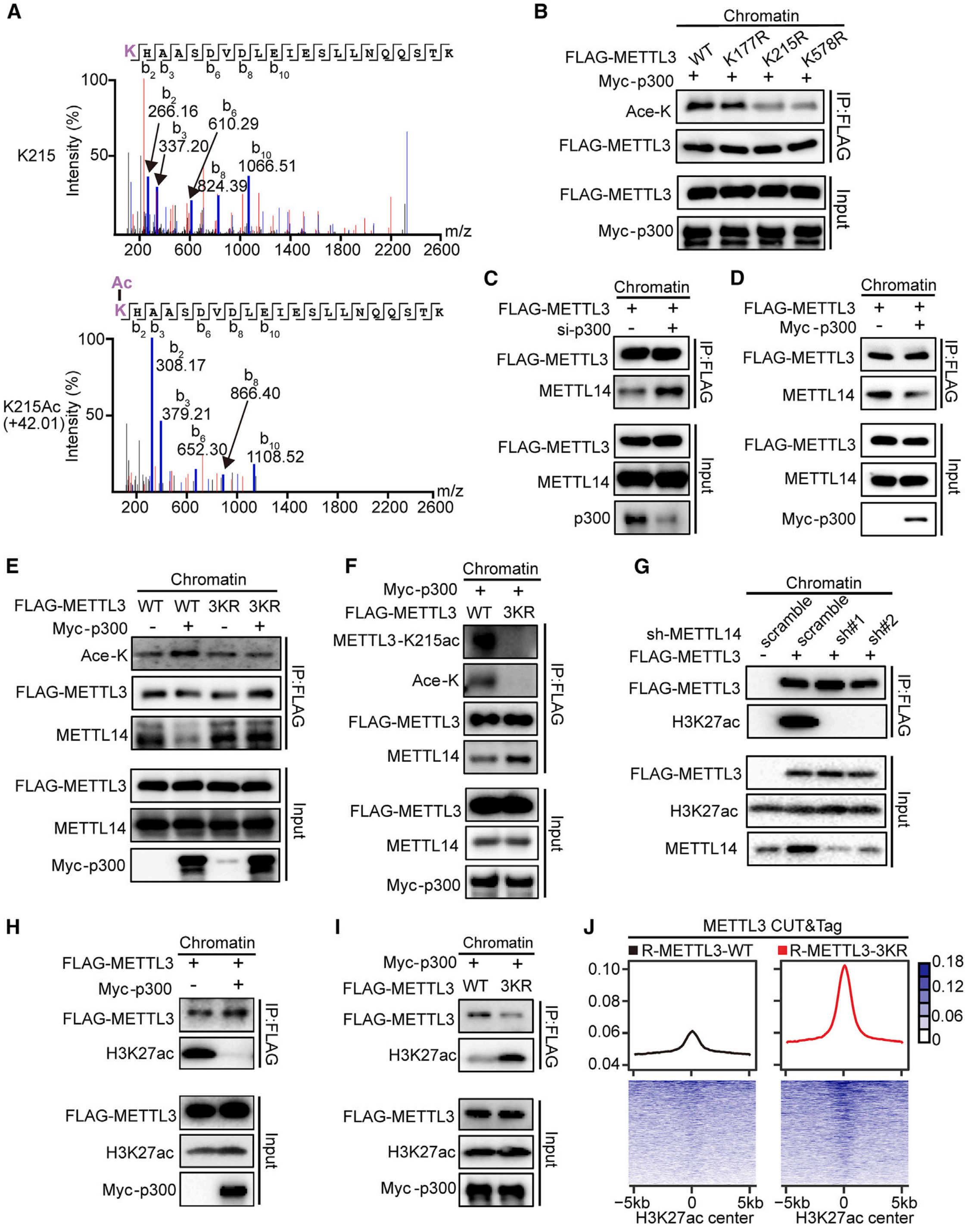

Figure 3. METTL3 acetylation prohibits the localization of METTL3 on H3K27ac-marked chromatin by inhibiting the interaction between METTL3 and METTL14 on chromatin

(A) Mass spectrum analysis detects chromatin-associated METTL3 acetylation site.

(B) Chromatinic lysates of HEK293T cells, transfected as indicated, were analyzed by coIP to detect METTL3 acetylation.

(C and D) Chromatinic lysates of HEK293T cells, transfected as indicated, were analyzed by coIP to detect METTL3-METTL14 interaction.

(E and F) Chromatinic lysates of HEK293T cells, transfected as indicated, were analyzed by coIP to detect METTL3-METTL14 interaction, METTL3 acetylation, and METTL3-K215 acetylation.

(G) Chromatinic lysates of sh-scramble or sh-METTL14 HEK293T cells, transfected as indicated, were analyzed by coIP to detect METTL3-H3K27ac interaction.

(legend continued on next page)

METTL3 acetylation, respectively. Consistent with the previous study,[30] the METTL3-K177R mutation could significantly reduce the p300-mediated METLL3 acetylation (Figure 3B). In addition, we also identified that METTL3-K215R and METTL3-K578R mutation could also result in a significant reduction in p300-mediated chromatin-associated METTL3 acetylation, rather than K to R mutation on K211 and K327 sites of chromatin-associated METTL3 (Figures 3B and S3F). These results indicated that K177, K215, and K578 are acetylation sites of METTL3 catalyzed by p300 on chromatin.

p300-mediated METTL3 acetylation inhibits its interaction with METTL14 on chromatin

Through coIP in the isolated chromatin fraction of HEK293T cells, we found that knockdown of *EP300* other than its close homolog *CBP* (CREB-binding protein) increased the interaction between METTL3 and METTL14 on chromatin (Figures 3C and S3G); while p300 overexpression significantly decreased the interaction between METTL3 and METTL14 on chromatin (Figure 3D). Together, these results demonstrated that p300 inhibits the interaction of METTL3 with METTL14 on chromatin.

Next, we mutated all three lysine at K177, K215, and K578 of METTL3 to arginine (METTL3-3KR) to mimic the non-acetylation status. As expected, overexpression of p300 enhanced the acetylation of chromatin-associated wild-type (WT) METTL3, but not the METTL3-3KR mutant (Figure 3E). Similarly, the chromatin-associated interaction of METTL14 with WT METTL3, but not the METTL3-3KR mutant, is inhibited by p300 overexpression in HEK293T cells (Figure 3E). We then mutated the three lysine of METTL3 to glutamine (METTL3-3KQ) to mimic the lysine acetylation status as previously reported.[41] In contrast to the 3KR mutation, the 3KQ mutation had an obvious inhibitory effect on METTL3 binding with METTL14 on chromatin (Figure S3H). We then generated an acetylation-K215-METTL3-specific antibody due to its higher technical applicability compared with K177 and K578. Based on ELISA and western blot, we confirmed that the acetylation-K215-METTL3-specific antibody specifically recognizes K125ac other than unmodified K125, nor other acetylation sites or other proteins (Figures S3I–S3K). Subsequently, by using this antibody, we observed that p300 promotes endogenous chromatin-associated METTL3 acylation at the K215 site (Figure S3L). We then found that METTL3-3KR mutant dramatically decreases chromatin-associated METTL3 acetylation at the K215 site and increases chromatin-associated METTL3 interacting with METTL14 (Figure 3F). Similar results were observed in A549 cells (Figures S4A and S4B). Collectively, these results demonstrated that acetylation of METTL3 by p300 inhibits its interaction with METTL14 on chromatin.

Acetylation of METTL3 inhibits METTL3 deposition on H3K27ac-bound chromatin

A previous study reported that METTL3, METTL14, and WTAP are mainly located in regions of enhancers and promoters, which are marked by H3K27ac as well as p300 binding.[21] Consistently, within the isolated chromatin fractions, we found that METTL3 binds with H3K27ac in an RNA-independent manner in HEK293T cells (Figure S4C). Furthermore, METTL14 knockdown remarkably suppressed the interaction of METTL3 with H3K27ac on chromatin (Figure 3G). These results indicate that interacting with METTL14 is required for METTL3 to localize on H3K27ac-marked chromatin, which is similar to the previous report that METTL14 mediates the binding of METTL3 to H3K36me3 marked chromatin.[20]

We were then interested in whether the acetylation of METTL3 affects its localization on H3K27ac-marked chromatin. We found that p300 overexpression inhibits the interaction between METTL3 and H3K27ac (Figure 3H). However, p300 overexpression only moderately decreases the abundance of chromatin METTL3 and increases nucleoplasmic METTL3, implying that acetylated METTL3 by p300 may relocate to other chromatin loci and serve as a regulator independent of METTL14 or its methylation activity (Figure S4D). Moreover, METTL3-3KR mutation promoted the interaction between METTL3 and H3K27ac (Figure 3I). Similar results were also observed in A549 cells (Figures S4E and S4F). To further investigate whether METTL3 acetylation regulates the re-distribution of METTL3 and H3K27ac on chromatin, we first knockdown endogenous METTL3 in A549 cells and rescued the cells by overexpression METTL3-WT and METTL3-3KR to a similar level of METTL3 protein as the WT A549 cells (Figure S4G). Then, we performed CUT&Tag (cleavage under targets and tagmentation)[42] for METTL3 binding as well as H3K27ac in the METTL3-WT-rescued and METTL3-3KR-rescued A549 cells, respectively. As compared with WT METTL3, METTL3-3KR showed much higher METTL3-binding signals at H3K27ac-marked chromatin regions other than H3K36me3 or H3K9me3 marked regions (Figures 3J and S5A). We then identified 10,215 upregulated and 346 downregulated METTL3-binding peaks upon METTL3-3KR mutation in A549 cells (Figure S5B). The upregulated other than the downregulated METTL3-binding peaks in METTL3-3KR were significantly enriched near transcription start sites (TSSs) (Figures S5C and S5D). Consistently, the upregulated METTL3 binding peaks in METTL3-3KR were also significantly enriched in H3K27ac-bound chromatin compared with unchanged or downregulated peaks (Figure S5E). On the other hand, in contrast to METTL3 CUT&Tag signals, we did not observe significant changes of H3K27ac CUT&Tag signal between METTL3-3KR and METTL3-WT at TSSs or METTL3 binding regions, which is consistent with our proposed model that acetylation of METTL3 directly regulates the location of METTL3 (Figures S5F and S5G). However, when we looked at the upregulated METTL3 peaks in METTL3-3KR, we found they had marginally but significantly lower fold changes of H3K27ac signals between METTL3-3KR and METTL3-WT (Figure S5H), suggesting that 3KR mutations of METTL3 may have indirect effects of suppressing the transcription activities of

(H and I) Chromatinic lysates of HEK293T cells, transfected as indicated, were analyzed by coIP to detect METTL3-H3K27ac interaction.

(J) Profiles of METTL3 on H3K27ac-bound chromatin, spanning 5 kb upstream and 5 kb downstream of the H3K27ac peak center, in A549 cells rescued with METTL3-WT or METTL3-3KR.

See also Figures S3–S5.

Please cite this article in press as: Huang et al., Spatial control of m^{6}A deposition on enhancer and promoter RNAs through co-acetylation of METTL3 and H3K27 on chromatin, Molecular Cell (2025), https://doi.org/10.1016/j.molcel.2025.02.016

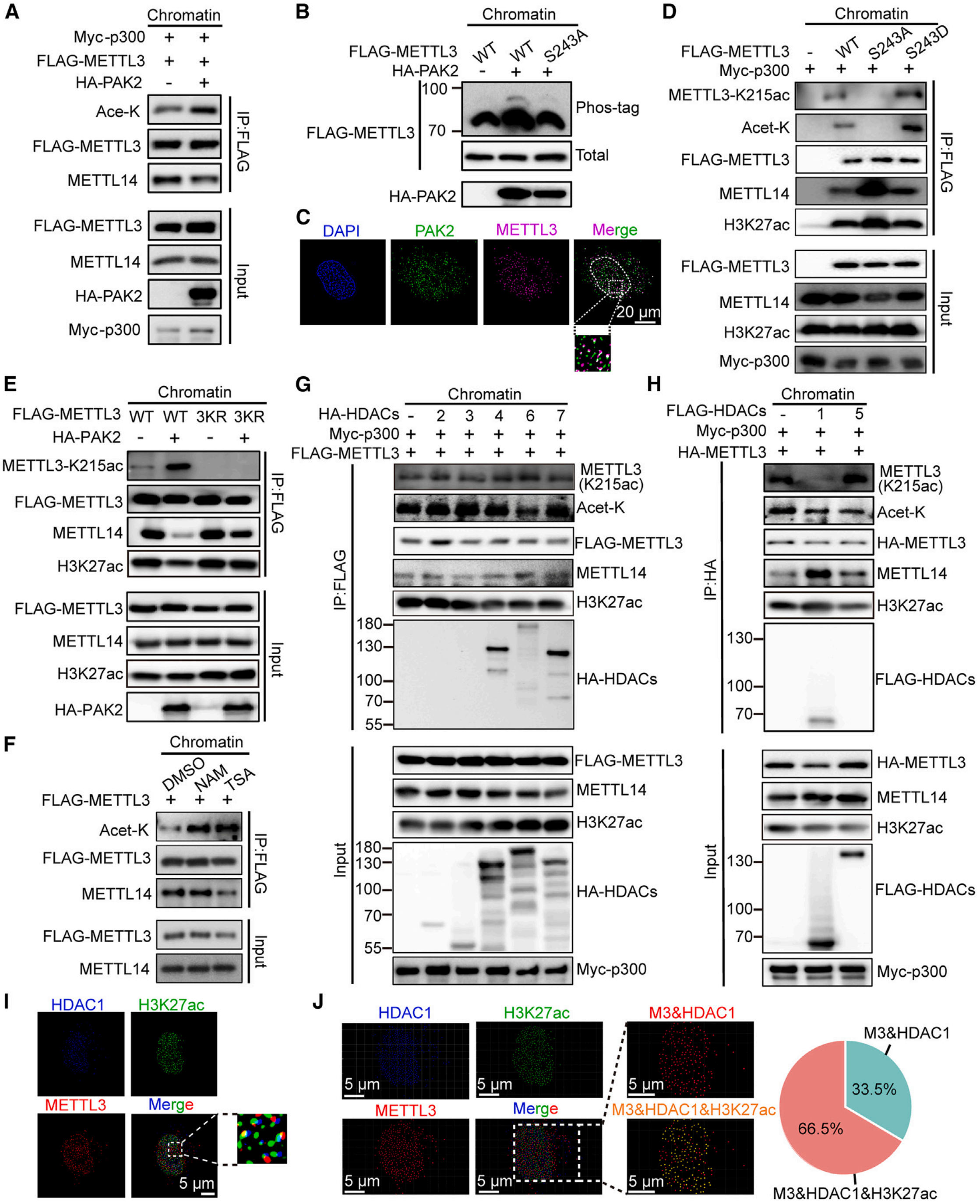

Figure 4. PAK2 and HDAC1 are regulators of METTL3 acetylation

(A) Chromatinic lysates of HEK293T cells, transfected as indicated, were analyzed by coIP to detect METTL3-METTL14 interaction and METTL3 acetylation.

(B) Chromatinic lysates of HEK293T cells, transfected as indicated, were analyzed by Phos-tag SDS-PAGE to detect METTL3 phosphorylation.

(C) 3D-SIM was used to detect localization of METTL3 (purple) and PAK2 (green) in HEK293T cells. DAPI (blue) was used to mark the nucleus. Scale bars, 20 μm.

(D and E) Chromatinic lysates of HEK293T cells, transfected as indicated, were analyzed by coIP to detect METTL3-METTL14 interaction, METTL3-H3K27ac interaction, METTL3 acetylation, and METTL3-K215ac acetylation.

(F) Chromatinic lysates of FLAG-tagged METTL3 overexpression HEK293T cells, treated with 2.5 mM NAM or 1 μM TSA for 16 h, were analyzed by coIP to detect METTL3-METTL14 interaction and METTL3 acetylation.

(G and H) Chromatinic lysates of HEK293T cells, transfected as indicated, were analyzed by coIP to detect METTL3-METTL14, METTL3-H3K27ac, METTL3-HDAC interaction, and METTL3 acetylation.

(I) 3D-SIM was used to detect the localization of HDAC1 (blue), METTL3 (red), and H3K27ac (green) in HEK293T cells. Scale bars, 5 μm.

(legend continued on next page)

certain genes.[2] Collectively, these results indicate that METTL3 acetylation prohibits the localization of METTL3 on H3K27ac-marked chromatin by inhibiting the interaction between METTL3 and METTL14 on chromatin.

PAK2 facilitates p300-mediated METTL3 acetylation by mediating METTL3 phosphorylation

According to the above genome-wide screening, several protein kinases, especially PAK2, can also inhibit the interaction between METTL3 and METTL14 (Figure 1D). Consistent with the previous reports that phosphorylation can crosstalk with acetylation,[35] we found that PAK2 overexpression not only decreased the interaction between METTL3 and METTL14 on chromatin but also increased the acetylation of chromatin-associated METTL3 in HEK293T cells, suggesting that PAK2 may affect the METTL3 acetylation through phosphorylating METTL3 (Figure 4A). In addition, GPS, a software that predicts phosphorylation sites with potential kinases,[43] predicted that METTL3 is phosphorylated at S243 by PAK2 (Figure S6A). Mass spectrometry analysis also revealed that S243 is a potential phosphorylation site (Figure S6B). Moreover, protein sequence alignment of METTL3 homologs showed that S243 is evolutionarily conserved in vertebrates (Figure S6C). To confirm whether PAK2 promotes the acetylation of chromatin-associated METTL3 by phosphorylating METTL3 at the S243 site, we performed a Phos-tag gel assay and found that overexpression of PAK2 increased the phosphorylation-dependent mobility shift of WT METTL3 but not the mutant METTL3-S243A serine to alanine,[44] which could mimic the phospho-inactive at S243 (Figure 4B). In addition, we also confirmed that PAK2 interacts with METTL3 (Figure S6D). The co-localization of PAK2 and METTL3 was also observed using 3D-SIM (Figure 4C). We further found that the disruptive S243A mutation dramatically decreases chromatin-associated METTL3 acetylation and promotes the interaction of chromatin-associated METTL3 with METTL14 and H3K27ac, whereas the S243D serine to aspartate mutation, which could mimic the phospho-active at S243, dramatically increased chromatin-associated METTL3 acetylation (Figure 4D). Similar results were also observed in A549 cells (Figures S6E–S6G). In addition, the inhibited interaction between METTL3 with METTL14 and H3K27ac on chromatin by overexpression of PAK2 was attenuated by METTL3-3KR mutations (Figure 4E), suggesting that PAK2 regulates the interaction between METTL3 with METTL14 and H3K27ac partially depends on the acetylation of METT3. Collectively, these results indicate that PAK2 inhibits the interaction of METTL3 with METTL14 and H3K27ac by promoting METTL3 phosphorylation, which in turn facilitates METTL3 acetylation on H3K27ac-marked chromatin.

HDAC1 deacetylates METTL3

Next, to identify the deacetylase that targets K177, K215, and K578 sites on METTL3, we used the deacetylase inhibitors TSA and NAM to determine whether the two classes of deacetylases HDACs and SIRTs are involved in the deacetylation of chromatin-associated METTL3, respectively. Treatment of HEK293T cells with the HDAC inhibitor TSA and the SIRT inhibitor NAM both increased the acetylation of chromatin-associated METTL3. However, only the HDAC inhibitor TSA, but not the SIRT inhibitor NAM, inhibited the interaction between METTL3 and METTL14 on chromatin (Figure 4F). Thus, the HDACs family may be preferentially involved in METTL3 deacetylation at K177, K215, and K578 sites. We then attempted to identify which members of the HDACs family are involved in chromatin-associated METTL3 deacetylation. We overexpressed HDAC1, HDAC2, HDAC3, HDAC4, HDAC5, HDAC6, and HDAC7 and found that only overexpression of HDAC1, the deacetylase of H3K27ac,[45] increased the interaction between METTL3 with METTL14 and H3K27ac on chromatin (Figures 4G and 4H). We further found that METTL3 co-localizes with HDAC1 and H3K27ac (Figure 4I). Microscopy image analysis[39] showed that 66.5% of HDAC1-bound METTL3 simultaneously co-localizes with H3K27ac (Figure 4J). Similar results were also observed in A549 cells (Figures S6H and S6I). Together, these data indicate that HDAC1 is a deacetylase of H3K27ac-bound METTL3 and promotes the interaction between METTL3 and METTL14 on H3K27ac-marked chromatin.

METTL3 acetylation inhibits m^{6}A deposition on eRNAs and paRNAs to enhance gene expression

We next investigated whether the association of METTL3 on H3K27ac-marked chromatin regulated by the METTL3 acetylation could affect the m^{6}A of chromatin RNAs transcribed from H3K27ac-marked chromatin. A previous study revealed that METTL3-K177Q, other than METTL3-K177R mutation, can inhibit the nuclear translocation of METTL3.[30] Here, we also observed that METTL3-3KR could not affect the nuclear translocation of METTL3 (Figure S7A). Then, we used GLORI-seq (glyoxal and nitrite-mediated deamination of unmethylated adenosine sequencing)[46] to identify and quantify the single-nucleotide m^{6}A sites on the chromatin-associated RNAs (caRNAs). We optimized the previous protocol[46] (see STAR Methods) and increased the lengths of inserted fragments of the libraries with A-to-I conversion rates ranging from 97.69% to 98.45%. Similar to the previously published caRNA-seq data in HepG2 cells,[23] our caRNA-seq data in A549 cells have on average 66.70% and 5.38% of reads uniquely mapped to intronic and intergenic regions, respectively, which is distinctive from our mRNA-seq data in A549 cells (Figure S7B). In addition, our GLORI-seq revealed that the m^{6}A levels were reproducible (Figure S7C), and 34,193 and 37,917 common m^{6}A sites were identified in A549 cells rescued with METTL3-WT and METTL3-3KR, respectively. 84% of these m^{6}A sites were within the DRACH motif (D = A\G\U, R = A\G, H = A\C\U), suggesting our GLORI-seq data are reliable (Figure S7D). For the METTL3-WT samples, 14.99%, 5.8%, and 7.37% of the m^{6}A sites were located in introns, promoters, and intergenic regions, respectively

(J) The spot model of Imaris software was used to reconstruct HDAC1, METTL3, and H3K27ac based on 3D-SIM data (left), which was used to calculate their co-localization relationship. The fractions of METTL3 proteins colocalize with both HDAC1 and H3K27ac (M3 & HDAC1 & H3K27ac), as well as the METTL3 proteins only colocalize with HDAC1 but not H3K27ac (M3 & HDAC1), are depicted in the pie chart (right).
See also Figure S6.

Please cite this article in press as: Huang et al., Spatial control of m^6A deposition on enhancer and promoter RNAs through co-acetylation of METTL3 and H3K27 on chromatin, Molecular Cell (2025), https://doi.org/10.1016/j.molcel.2025.02.016

(Figure S7E); the METTL3-3KR samples had similar compositions. Consistent with the previous study using MeRIP-seq (m^6A-specific methylated RNA immunoprecipitation with next-generation sequencing),[47] our results also showed that intronic m^6A sites on chromatin RNAs were overrepresented near splice junctions (SJs) (Figure S7F). Consistent with the finding that METTL3 acetylation inhibits m^6A deposition, we identified 1,541 upregulated and only 839 downregulated m^6A sites in A549 cells rescued with METTL3-3KR (Figure S7G; Table S2).

To study the association between m^6A and histone modifications, we then collected the chromatin immunoprecipitation sequencing (ChIP-seq) data in A549 cells from ENCODE (Encyclopedia of DNA Elements) and GEO database,[48–53] including p300, H3K9me3 that marks heterochromatin, H3K36me3 that marks gene bodies, H3K27ac that marks both active enhancers and promoters, H3K4me1 that marks active enhancers with H3K27ac, H3K4me2, and H3K4me3 that marks active promoters with H3K27ac that marks active promoters, as well as the binding regions of p300, which is the acetylase of H3K27ac.[37,54–56] We found that in the cells rescued by METTL3-WT, the m^6A levels in the regions marked by H3K9me3 and H3K36me3 were much higher than those marked by H3K4me1, H3K4me2, H3K4me3, H3K27ac, as well as p300-binding regions (Figure S8A). This result is consistent with the previous reports that m^6A has crosstalk with H3K9me3 and H3K36me3.[20,57] Nevertheless, when we looked at the changes of m^6A levels resulting from 3KR mutations of METTL3, we found a different scenario: m^6A sites in H3K4me1-, H3K4me2-, H3K4me3-, H3K27ac-marked regions, as well as p300-binding regions other than those in H3K9me3- and H3K36me3-marked regions were more notably upregulated by 3KR mutations (Figures 5A and S8B; Table S2). Consistently, the highly m^6A methylated m^6A sites had notably lower p300-binding efficiencies in H3K27ac-bound regions, but not in H3K36me3 and H3K9me3 regions (Figures 5B and S8C). In addition, we also found that the m^6A levels of these intergenic m^6A sites closer to p300-binding peaks had a significantly lower m^6A level than those further away from p300-binding peaks (Figure 5C). Similar to H3K27ac, we also observed that H3K4me1 and H3K4me3 were co-localized with METTL3 (Figure S8D). RNA-independent interaction of H3K4me1 and H3K4me3 with chromatin-associated METTL3 was also observed, whereas METTL14 knockdown could dramatically inhibit the interaction of H3K4me1 and H3K4me3 with METTL3 (Figures S8E and S8F). Moreover, p300 overexpression could inhibit the binding of chromatin-associated METTL3 with H3K4me1 and H3K4me3, whereas METTL3-3KR mutations increased these interactions (Figures S8G and S8H). These results suggest that the METTL3 acetylation specifically inhibits the m^6A on RNAs transcribed from enhancers and promoters.

We then determined the eRNAs and paRNAs based on the enhancer regions and promoter regions defined by histone modifications. In cells rescued with METTL3-WT, we identified 2,532 and 752 m^6A sites on eRNAs and paRNAs, respectively. The m^6A on eRNAs were significantly ($p = 4.2 \times 10^{-4}$, two-tailed Wilcoxon test) upregulated upon 3KR mutations, whereas trend of upregulation ($p = 7.6 \times 10^{-2}$, two-tailed Wilcoxon test) was also observed for paRNAs possibly due to the relatively fewer m^6A sites on paRNAs (Figure 5D). In addition, we also observed that the changes of METTL3 binding between METTL3-3KR and METTL3-WT were significantly higher in chromatin regions associated with m^6A-upregulated RNAs, especially with upregulated eRNAs and paRNAs, compared with all regions (Figure 5E). Consistent with the previous report that the m^6A on eRNAs and paRNAs promotes the degradation of these RNAs to suppress gene expression,[2] we also found eRNAs and paRNAs abundances were downregulated by 3KR mutations (Figure S8I). Furthermore, METTL3-3KR mutations resulted in significantly greater downregulation of the expression of m^6A-upregulated eRNAs, as compared with the m^6A-downregulated, m^6A-unchanged, and non-modified eRNAs (Figure 5F; Table S3). Similar downregulation was also observed for the expression of the mRNAs associated with the m^6A-upregulated eRNAs other than those associated with other eRNAs (Figure 5G; Table S4). We also found similar results in paRNAs (–) (Figures S8J and S8K; Tables S3 and S4). These results suggest that 3KR mutations of METTL3 result in upregulated m^6A and downregulated stabilities of eRNAs and paRNAs, as well as downregulated expression of their associated mRNAs.

METTL3 acetylation inhibits ferroptosis by inhibiting the m^6A on eRNAs and paRNAs

We found that the associated genes of these eRNAs and paRNAs with upregulated m^6A sites were significantly enriched in the pathways amplified in lung cancer, as well as some specific pathways widely recognized as ferroptosis pathway and ferroptosis related, such as oxidoreductase activity, unsaturated fatty acid metabolic process, steroid metabolic process, and NRF2 pathway, which is a known ferroptosis-inhibited pathway[58] (Figure 6A; Table S3). Further, we found that downregulated mRNAs upon 3KR mutations were also significantly enriched in the NRF2 pathway (Figure S9A; Table S4). As shown in Figure 6B, the m^6A on the eRNAs of *AKR1C1* and *AKR1C2*, two representative genes in the NRF2 and ferroptosis pathway, were elevated upon METTL3-3KR mutations, in company with downregulated expression of these eRNAs (Figure 6B). Based on quantitative real-time PCR, we found significant mRNA expression downregulation of 6 representative ferroptosis-inhibition-related genes that were associated with eRNAs containing upregulated m^6A sites upon METTL3-3KR mutations (Figure 6C). Next, we treated A549 cells with ferroptosis-inducer ML162 and RSL3, and observed that METTL3-3KR mutations promoted ML162 and RSL3-induced cell death and lipid peroxidation, whereas ferrostatin-1 (Fer-1), a ferroptosis inhibitor, rescued cell death promoted by METTL3-3KR mutations (Figures 6D, 6E, and S9B). Collectively, these results indicate that the acetylation of chromatin-associated METTL3 inhibits ferroptosis by inhibiting the m^6A of eRNAs and paRNAs associated with genes that inhibit ferroptosis.

PAK2 inhibitor promotes ferroptosis depending on the acetylation of METTL3

PAK (p21-activated kinase) family members are known as oncogenes and are highly expressed in multiple types of tumors; antitumor drugs targeting the PAK family are under development.[36,59] Our study uncovered an uncharacterized oncogenic

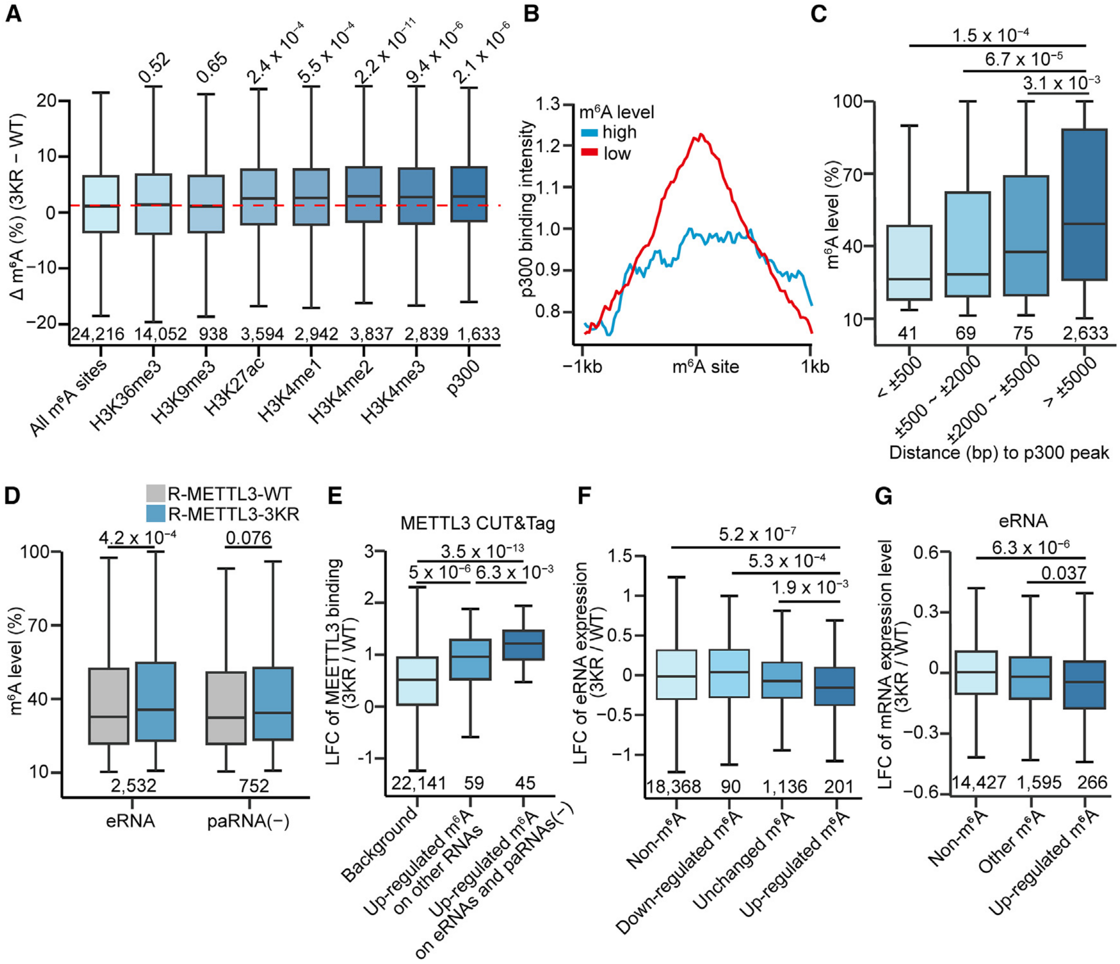

Figure 5. METTL3 acetylation inhibits m^{6}A deposition on eRNAs and paRNAs to promote downstream gene expression

(A) Boxplot comparing m^{6}A level differences in METTL3-3KR-rescued A549 cells versus METTL3-WT-rescued controls at different genomic regions. m^{6}A sites were grouped based on overlap with H3K36me3, H3K9me3, H3K4me1, H3K4me2, H3K4me3, H3K27ac, or p300 peaks. The number and *p* value of each category are indicated below and above the boxplot, respectively. *p* values were calculated by two-sided Wilcoxon rank-sum test.

(B) Profiles of p300 binding within 1 kb of the genomic locations of highly (level > 0.5) and lowly (level < 0.5) methylated m^{6}A sites located within H3K27ac-marked regions in A549 cells.

(C) Boxplot comparing the levels of intergenic m^{6}A sites with different distances to p300 peaks center in A549 cells. The number of each category m^{6}A site is indicated below the boxplot. *p* values were calculated by two-sided Wilcoxon rank-sum test.

(D) Boxplot comparing the m^{6}A levels in METTL3-3KR-rescued A549 cells versus METTL3-WT-rescued controls for m^{6}A sites on eRNAs ($n = 2{,}532$) and paRNAs (–) ($n = 752$), respectively. *p* values were calculated by two-sided Wilcoxon rank-sum test.

(E) Boxplot comparing the $\log_2$ fold change (LFC) of METTL3-binding intensity in METTL3-3KR-rescued A549 cells versus METTL3-WT-rescued controls. METTL3 peaks were categorized into two groups based on their overlap with upregulated m^{6}A sites on either eRNAs/paRNAs (–) or other RNAs. The number of METTL3 peaks in each category is indicated below the boxplot. *p* values were calculated by two-sided Wilcoxon rank-sum test.

(F) Boxplots comparing the LFC of eRNA expression in METTL3-3KR-rescued A549 cells versus METTL3-WT-rescued controls. eRNAs were classified into four categories: those lacking m^{6}A sites, those with downregulated m^{6}A sites, those with upregulated m^{6}A sites, and those containing unchanged m^{6}A sites. The number of eRNAs in each category is indicated below the boxplot. *p* values were calculated by two-sided Wilcoxon rank-sum test.

(G) Boxplot comparing the LFC of the eRNA-associated mRNA expression in METTL3-3KR-rescued A549 cells versus METTL3-WT-rescued controls. mRNAs were grouped based on the m^{6}A status of their associated eRNAs: eRNAs with upregulated m^{6}A, eRNAs with non-upregulated m^{6}A, and eRNAs without m^{6}A sites. The number of mRNAs in each category is indicated below the boxplot. *p* values were calculated by two-sided Wilcoxon rank-sum test.

See also Figures S7 and S8 and Tables S2, S3, and S4.

role of PAK2 by inhibiting ferroptosis depending on the acetylation of METTL3. Interestingly, based on The Cancer Genome Atlas (TCGA) data, we found that lung adenocarcinoma (LUAD) patients whose tumors expressed low levels of PAK2 had a better prognosis than those with higher PAK2 expression only in patients with METTL3 high expression, other than patients with METTL3 low expression (Figure 7A). Similar results were also observed in liver carcinoma (LIHC), papillary renal cell carcinoma (KIRP), bladder carcinoma (BLCA), and colorectal carcinoma (COAD) (Figure S10A). These results further support the

Please cite this article in press as: Huang et al., Spatial control of m^{6}A deposition on enhancer and promoter RNAs through co-acetylation of METTL3 and H3K27 on chromatin, Molecular Cell (2025), https://doi.org/10.1016/j.molcel.2025.02.016

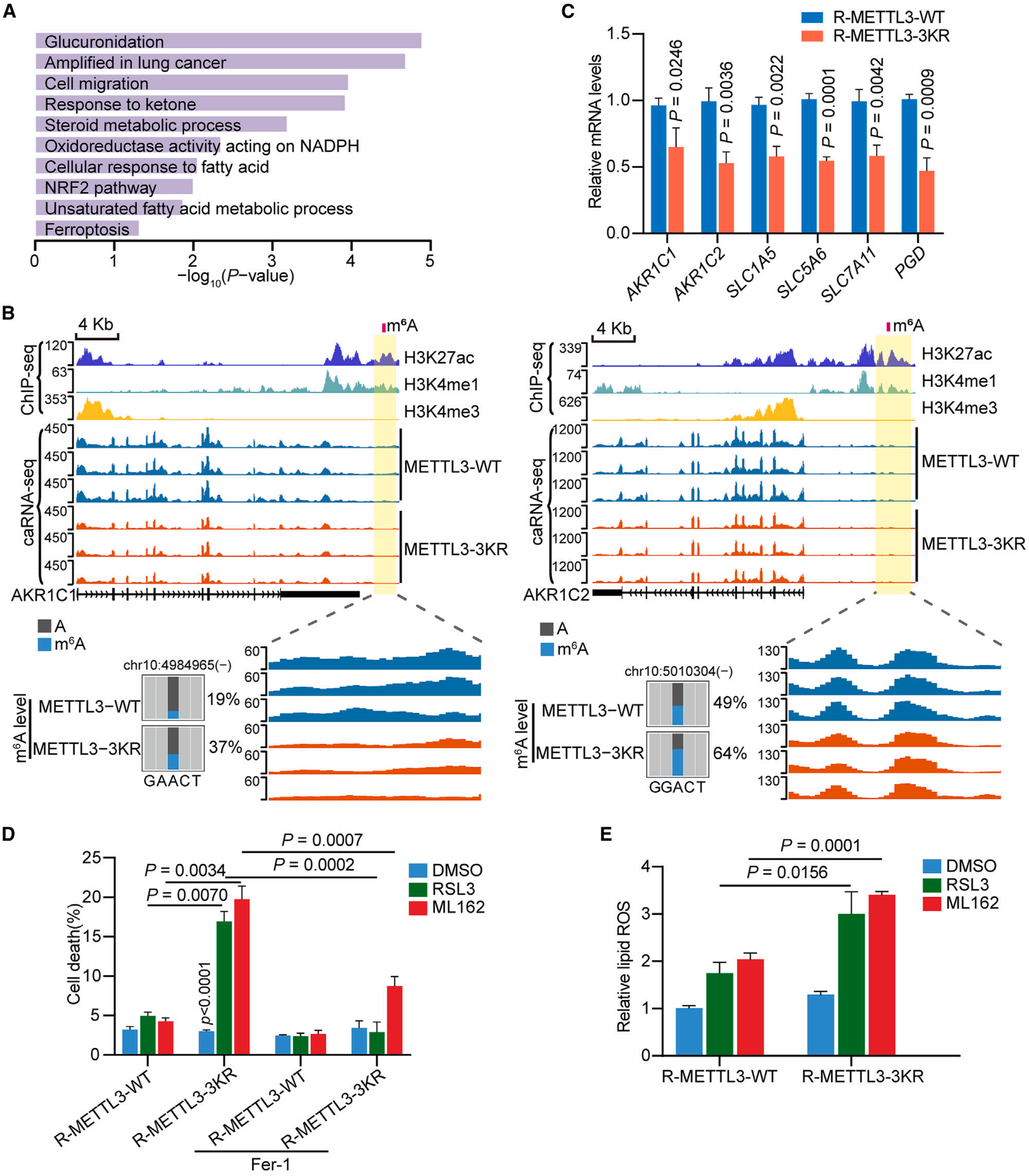

Figure 6. METTL3 acetylation inhibits ferroptosis by inhibiting eRNAs and paRNAs m^{6}A methylation

(A) Functional enrichment analysis of genes with m^{6}A-up-regulated eRNAs and paRNAs (–) was executed by MsigDB (Molecular Signatures Database). *p* values were calculated by one-sided hypergeometric test.

(B) The m^{6}A level and eRNA level in A549 cells around the *AKR1C1* and *AKR1C2* gene locus are shown by integrative genomics viewer plots.

(C) Bar plot comparing the quantitative real-time PCR measured mRNA abundances of representative ferroptosis-related genes in METTL3-3KR-rescued A549 cells versus METTL3-WT-rescued controls. Data are presented as mean ± SD (*n* = 3 independent experiments). *p* values were calculated by two-tailed unpaired Student's t tests.

(legend continued on next page)

METTL3-dependent role of PAK2 in promoting the survival of cancer cells.

On the other hand, accumulating evidence revealed that cancer cells have higher iron metabolic demands, making them more susceptible than normal cells to ferroptosis. Thus, ferroptosis plays a key role in tumor suppression, and agents that induce ferroptosis have been described as potential adjuvant anti-cancer treatments.[58] Notably, we found that FRAX486, a PAK2 inhibitor, could increase ML162- and RSL3-induced cell death and lipid peroxidation in A549 cells with WT METTL3, whereas the ferroptosis inhibitor Fer-1 rescued FRAX486 promoted ML162 and RSL3-induced cell death (Figures 7B, 7C, and S10B). METTL3-3KR mutations had a similar effect as FRAX486 and almost completely suppressed the effects of FRAX486 on ML162 and RSL3-induced cell death. Similar results were also observed in HepG2, a liver cancer cell line (Figures S10C–S10E). Besides RSL3 and ML162, there is also a first-line drug, cisplatin (CDDP), that is known to promote cell death by inducing apoptosis and ferroptosis.[60] CDDP is being used in the therapy of numerous tumors, including lung carcinoma, BLCA, and colorectal carcinoma.[61] We found the PAK2 inhibitor FRAX486 could also promote the antitumor effects of CDDP on cell death as well as lipid peroxidation in A549 cells with WT METTL3 other than METTL3-3KR mutant, suggesting the PAK2 inhibitor promotes the antitumor efficiency of CDDP through the acetylation of METTL3 (Figures 7D, 7E, and S10F).

DISCUSSION

METTL3 acetylation mediates the external stimulation-induced specific m^{6}A changes

Our finding uncovered an uncharacterized mechanism in which the acetylation of METTL3 works as a critical mediator for the external stimulations to confer selective cellular m^{6}A changes (Figure 7F). The m^{6}A on RNAs was widely known to be dynamically regulated, external stimulations, as well as different kinds of stresses can regulate m^{6}A specifically.[27,62–65] How these m^{6}A sites are selectively regulated is largely unknown. Here, we uncovered that the acetylation of METTL3 could be regulated by multiple kinases, which are important for sensing different types of external stimulations. The kinase-mediated dynamic acetylation of METTL3, thereby, provides a versatile platform for cells to coordinate the m^{6}A activity with diverse external environments.

Synergistic effect of p300-mediated chromatin opening and stabilization of enhancer and promoter RNAs

Our study uncovered an uncharacterized way of cooperative regulation of histone modification and m^{6}A modification through acetylating METTL3 by p300 on H3K27ac. Our study suggests that p300 activates gene expression through two different mechanisms. On one side, it opens the chromatin through H3K27ac; on the other side, it stabilizes the eRNAs and paRNAs transcribed from H3K27ac-marked chromatin to maintain the activity of enhancers. In addition, we also found that PAK2-mediated METTL3 phosphorylation promotes p300-mediated H3K27ac-bound METTL3 acetylation (Figure 7F); it bridges the gene activation on chromatin with kinase and possibly other cellular signal transduction pathways. Nevertheless, since the m^{6}A on eRNAs and paRNAs may also play transcription-promoting roles in certain cancer types,[21,22] the co-acetylation of H3K27 and METTL3 may also work as a negative feedback loop to maintain the homeostasis of gene expression.

Implication of METTL3 acetylation in precision medicine

Our data also imply that METTL3 acetylation can be used for precision medicine in cancer therapy. It is known that PAK family members are overexpressed and play oncogene roles in multiple types of cancers; a promising drug targeting PAK family members was in a phase I clinical trial of acute myeloid leukemia, non-Hodgkin's lymphoma, and advanced solid tumors.[59] Our study suggests that the acetylation of METTL3 should also be considered for precision medicine of certain cancers. On the other hand, the dual roles of METTL3 in both promoting and suppressing tumors were reported in different studies,[66] the acetylation of METTL3 may bridge the gap in understanding these seeming conflicts. The effects of METTL3 on cancers largely depend on whether they are acetylated, which further relies on the activities of other proteins, such as PAK2. Thus, the effects of METTL3, as well as m^{6}A, in cancers may be dependent on the cellular contexts that determine the acetylation levels of METTL3.

Multiple roles of acetylated METTL3 in the nucleus and cytoplasm

In contrast to our finding that acetylation of METTL3 mainly occurs in the nucleus, previous studies have reported controversial roles of cytosolic METTL3 acetylation.[30,31] In this study, we primarily focused on chromatin-bound METTL3 acetylation rather than METTL3 acetylation at the whole-cell level. This may largely explain why the role of METTL3 acetylation we identified is distinct from that reported in previous studies. Although METTL3 acetylation likely has dual roles in the cytoplasm and nucleus, p300-mediated METTL3 acetylation plays important roles in specifically regulating m^{6}A deposition on carRNAs transcribed from p300-bound chromatin.

Limitations of the study

Because p300-mediated METTL3 acetylation results in the dissociation of METTL3 from chromatin, we cannot rule out the possibility that the dissociated acetylated METTL3 may relocate to

---

(D) Bar plot comparing the cell death in METTL3-3KR-rescued A549 cells versus METTL3-WT-rescued controls, pre-treated with DMSO or Fer-1 (5 μM) for 12 h, and then treated with DMSO, RSL3 (5 μM), or ML162 (5 μM) for 24 h. Data are presented as mean ± SD (*n* = 3 independent experiments). *p* values were calculated by two-tailed unpaired Student's t tests.

(E) Bar plot comparing the lipid peroxidation in METTL3-3KR-rescued A549 cells versus METTL3-WT-rescued controls subjected to the indicated treatments for 12 h. RSL3, 5 μM; ML162, 5 μM. Data are presented as mean ± SD (*n* = 3 independent experiments). *p* values were calculated by two-tailed unpaired Student's t tests.

See also Figure S9 and Tables S2 and S3.

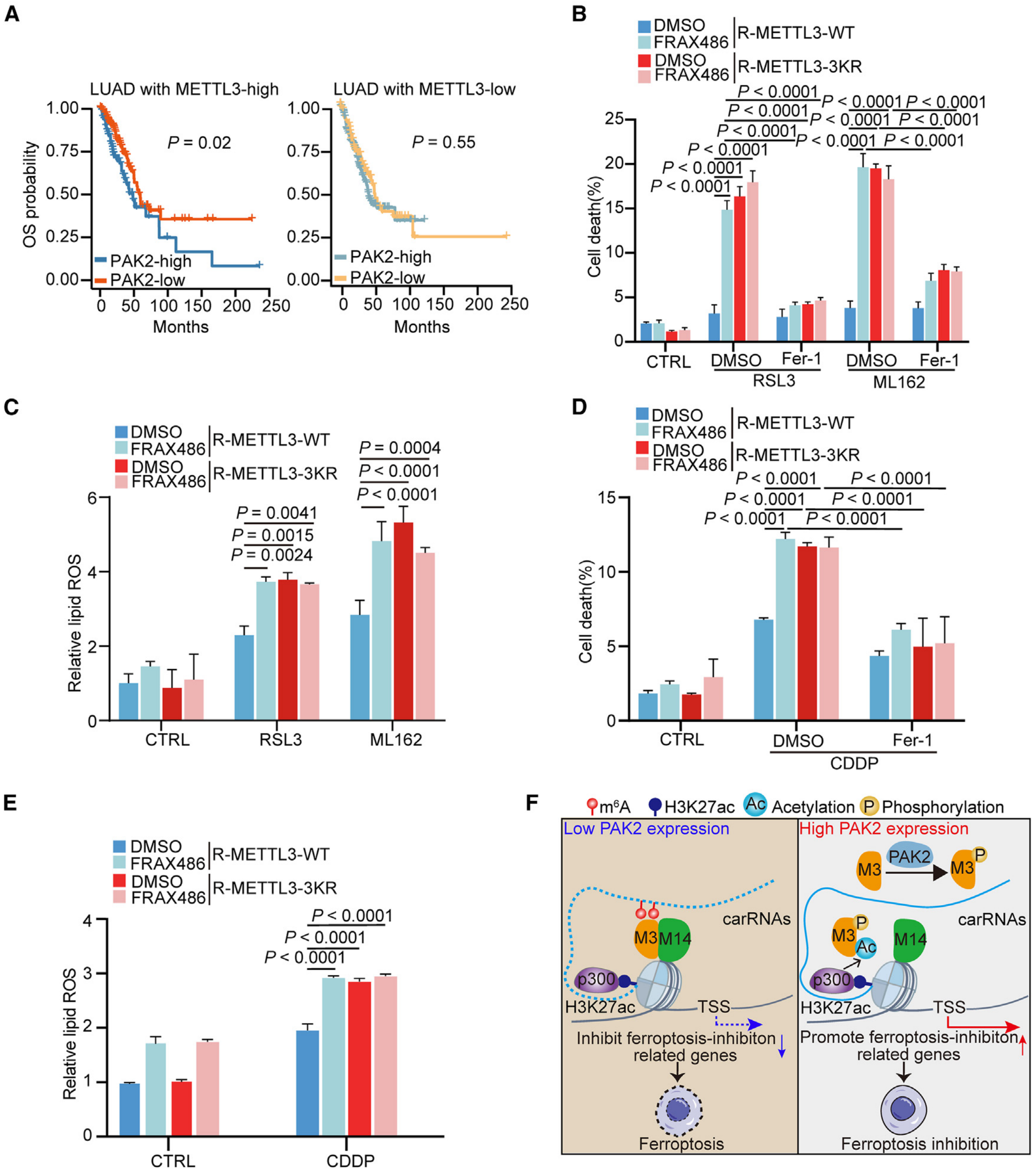

Figure 7. Pharmacologic targeting of PAK2 promotes ferroptosis in a METTL3-acetylation manner

(A) Kaplan-Meier survival analysis of TCGA datasets. The patients were divided into two groups according to METTL3 expression level, and each group was further divided into two groups according to PAK2 expression level. *p* values were calculated by log-rank test.

(B and C) Bar plot comparing the cell death (B) and lipid peroxidation (C) in METTL3-3KR-rescued A549 cells versus METTL3-WT-rescued controls, pre-treated with DMSO, FRAX486 (2 μM), or Fer-1 (5 μM) for 12 h, followed by treated with DMSO, RSL3 (5 μM), or ML162 (5 μM) for 24 h (B) or 12 h (C). Data are presented as mean ± SD (*n* = 3 independent experiments). *p* values were calculated by two-way ANOVA with Tukey's post hoc test.

(D and E) Bar plot comparing the cell death (D) and lipid peroxidation (E) in METTL3-3KR-rescued A549 cells versus METTL3-WT-rescued controls, pre-treated with DMSO, FRAX486 (2 μM), or Fer-1 (5 μM) for 12 h, followed by treated with PBS buffer or CDDP (90 μM) for 24 h (D) or 12 h (E). Data are presented as mean ± SD (n = 3 independent experiments). *p* values were calculated by two-way ANOVA with Tukey's post hoc test.

(F) A schematic model of the role of chromatin-associated METTL3 acetylation and phosphorylation by p300 and PAK2.

See also Figure S10.

other chromatin loci to methylate RNAs independent of METTL14 or serve as a regulator independent of its methylation activity. Indeed, recent studies suggest that METTL3 and METTL14 could be recruited to different genomic loci by various chromatin-binding proteins or histone modifiers. For example, only METTL3, but not METTL14, can be phosphorylated by ataxia telangiectasia mutated (ATM) kinase for localization to DNA damage sites for homologous recombination-mediated repair through m^{6}A,[27] whereas METTL14, but not METTL3, can interact with H3K27me3 and recruit KDM5B, KDM6B, and PRC2 to chromatin in an RNA- and m^{6}A-independent manner.[67,68] In human AML cells, METTL3, but not METTL14 also can be recruited to gene promoters through CEBPZ protein (CCAAT enhancer binding protein zeta) to facilitate m^{6}A deposition on nascent RNAs.[69] Alternatively, interaction between METTL3 and METTL14 also has m^{6}A-independent roles, which could also be regulated by METTL3 acetylation. It was also reported that interaction between METTL3 and METTL14 promotes the interaction between enhancers and promoters to drive the senescence-associated secretory phenotype independent of m^{6}A.[70] Thus, acetylation of METTL3 may play alternative roles in modulating the chromatin state for other cellular processes. The alternative roles of METTL3 acetylation will be further explored.

RESOURCE AVAILABILITY

Lead contact

Further information and requests for reagents should be directed to and will be fulfilled by the lead contact, Jinkai Wang (wangjk@mail.sysu.edu.cn).

Materials availability

All materials generated in this study are available from the lead contact upon request.

Data and code availability

The raw data produced during this study have been deposited into the GEO and Mendeley databases. They are publicly available as of the date of publication. The accession number is listed in the key resources table. Published datasets utilized in this study also are listed in the key resources table.

This paper does not report original code.

Any additional information required to reanalyze the data reported in this paper is available from the lead contact upon request.

ACKNOWLEDGMENTS

We thank the technical support of GLORI by Chengqi Yi and Hanxiao Sun, as well as the constructive advice from Xuan Li, Hailiang Zhang, and Jia Mai. This work was supported by the National Natural Science Foundation of China (32270630, to J.W.; 32300455, to Y.C.; 32100452, to X.S.), China Postdoctoral Science Foundation (2023M734053, to X.H.; 2024M753726, to Z.R.), the Guangdong Science and Technology Program (2022A1515110255, to Y.C.; 2024A1515011841, to J.W.; 2023A1515012495, to X.S.), and Guangzhou Science and Technology Program (SL2022A04J01057, to X.S.).

AUTHOR CONTRIBUTIONS

J.W. conceived and supervised the study; X.H., J.Z., and Y.C. performed most of the experiments with assistance from J.L., X.S., J.S., X.M., and X.Z.; M.Y. and Z.R. performed high-throughput sequencing data analyses with assistance from Z.W.; W.G. performed TCGA data analysis; W.L. provided support for sequencing; J.W. and X.H. wrote the manuscript.

DECLARATION OF INTERESTS

The authors declare no competing interests.

STAR★METHODS

Detailed methods are provided in the online version of this paper and include the following:

- KEY RESOURCES TABLE
- EXPERIMENTAL MODEL AND STUDY PARTICIPANT DETAILS
  - Cell culture
  - Antibodies and reagents
- METHOD DETAILS
  - Plasmids
  - Transfection and Virus Production
  - CRISPR-Cas9-mediated gene knockout
  - shRNA-mediated RNA interference
  - siRNA-mediated RNA interference
  - Genome-wide CRISPR/Cas9 screening
  - sgRNA sequencing data analysis
  - Western blotting and co-immunoprecipitation (co-IP)
  - Phosphate-affinity gel electrophoresis
  - Cell fractionation
  - Chromatin-associated protein co-immunoprecipitation
  - RNA extraction and quantitative real-time PCR
  - Chromatin-associated RNA (caRNA) extraction
  - GLORI-seq of chromatin-associated RNAs
  - caRNA-seq and RNA-seq
  - CUT&Tag
  - Mass spectrometry
  - Immunofluorescence staining and image analyses
  - Cell-death assays
  - Determination of lipid peroxidation
  - Enzyme-linked immunosorbent assay (ELISA assay)
  - GLORI-seq analysis for chromatin-associated RNAs
  - Determination of promoter and enhancer regions
  - mRNA-seq and caRNA-seq data analyses
  - ChIP-seq data and CUT&Tag data analyses
  - Gene ontology and pathway analyses
  - TCGA data analysis
- QUANTIFICATION AND STATISTICAL ANALYSIS

SUPPLEMENTAL INFORMATION

Supplemental information can be found online at https://doi.org/10.1016/j.molcel.2025.02.016.

Received: August 23, 2024
Revised: January 8, 2025
Accepted: February 19, 2025
Published: March 17, 2025

REFERENCES

1. Dominissini, D., Moshitch-Moshkovitz, S., Schwartz, S., Salmon-Divon, M., Ungar, L., Osenberg, S., Cesarkas, K., Jacob-Hirsch, J., Amariglio, N., Kupiec, M., et al. (2012). Topology of the human and mouse m^{6}A RNA methylomes revealed by m^{6}A-seq. Nature *485*, 201–206. https://doi.org/10.1038/nature11112.
2. Liu, J., Dou, X.Y., Chen, C.Y., Chen, C., Liu, C., Xu, M.M., Zhao, S.Q., Shen, B., Gao, Y.W., Han, D.L., et al. (2020). N6-methyladenosine of chromosome-associated regulatory RNA regulates chromatin state and transcription. Science *367*, 580–586. https://doi.org/10.1126/science.aay6018.
3. Wang, X., Zhao, B.S., Roundtree, I.A., Lu, Z.K., Han, D.L., Ma, H.H., Weng, X.C., Chen, K., Shi, H.L., and He, C. (2015). N(6)-methyladenosine Modulates Messenger RNA Translation Efficiency. Cell *161*, 1388–1399. https://doi.org/10.1016/j.cell.2015.05.014.
4. Shi, H.L., Wang, X., Lu, Z.K., Zhao, B.S., Ma, H.H., Hsu, P.J., Liu, C., and He, C. (2017). YTHDF3 facilitates translation and decay of N6-methyladenosine-modified RNA. Cell Res. *27*, 315–328. https://doi.org/10.1038/cr.2017.15.
5. Xiao, W., Adhikari, S., Dahal, U., Chen, Y.S., Hao, Y.J., Sun, B.F., Sun, H.Y., Li, A., Ping, X.L., Lai, W.Y., et al. (2016). Nuclear m(6)A Reader

YTHDC1 Regulates mRNA Splicing. Mol. Cell *61*, 507–519. https://doi.org/10.1016/j.molcel.2016.01.012.

6. Roundtree, I.A., Luo, G.Z., Zhang, Z.J., Wang, X., Zhou, T., Cui, Y.Q., Sha, J.H., Huang, X.X., Guerrero, L., Xie, P., et al. (2017). YTHDC1 mediates nuclear export of N^6-methyladenosine methylated mRNAs. eLife *6*, e31311. https://doi.org/10.7554/eLife.31311.
7. Wang, X., Lu, Z.K., Gomez, A., Hon, G.C., Yue, Y.N., Han, D.L., Fu, Y., Parisien, M., Dai, Q., Jia, G.F., et al. (2014). N6-methyladenosine-dependent regulation of messenger RNA stability. Nature *505*, 117–120. https://doi.org/10.1038/nature12730.
8. Liu, J.Z., Yue, Y.N., Han, D.L., Wang, X., Fu, Y., Zhang, L., Jia, G.F., Yu, M., Lu, Z.K., Deng, X., et al. (2014). A METTL3-METTL14 complex mediates mammalian nuclear RNA N6-adenosine methylation. Nat. Chem. Biol. *10*, 93–95. https://doi.org/10.1038/nchembio.1432.
9. Yue, Y.A., Liu, J., Cui, X.L., Cao, J., Luo, G.Z., Zhang, Z.Z., Cheng, T., Gao, M.S., Shu, X., Ma, H.H., et al. (2018). VIRMA mediates preferential m^{6}A mRNA methylation in 3′UTR and near stop codon and associates with alternative polyadenylation. Cell Discov. *4*, 10. https://doi.org/10.1038/s41421-018-0019-0.
10. Ping, X.L., Sun, B.F., Wang, L., Xiao, W., Yang, X., Wang, W.J., Adhikari, S., Shi, Y., Lv, Y., Chen, Y.S., et al. (2014). Mammalian WTAP is a regulatory subunit of the RNA N6-methyladenosine methyltransferase. Cell Res. *24*, 177–189. https://doi.org/10.1038/cr.2014.3.
11. Wen, J., Lv, R.T., Ma, H.H., Shen, H.J., He, C.X., Wang, J.H., Jiao, F.F., Liu, H., Yang, P.Y., Tan, L., et al. (2018). Zc3h13 Regulates Nuclear RNA m6A Methylation and Mouse Embryonic Stem Cell Self-Renewal. Mol. Cell *69*, 1028–1038.e6. https://doi.org/10.1016/j.molcel.2018.02.015.
12. Patil, D.P., Chen, C.K., Pickering, B.F., Chow, A., Jackson, C., Guttman, M., and Jaffrey, S.R. (2016). m^{6}A RNA methylation promotes XIST-mediated transcriptional repression. Nature *537*, 369–373. https://doi.org/10.1038/nature19342.
13. Wang, X., Feng, J., Xue, Y., Guan, Z.Y., Zhang, D.L., Liu, Z., Gong, Z., Wang, Q., Huang, J.B., Tang, C., et al. (2016). Structural basis of N(6)-adenosine methylation by the METTL3-METTL14 complex. Nature *534*, 575–578. https://doi.org/10.1038/nature18298.
14. Ke, S.D., Pandya-Jones, A., Saito, Y., Fak, J.J., Vågbo, C.B., Geula, S., Hanna, J.H., Black, D.L., Darnell, J.E., and Darnell, R.B. (2017). m^{6}A mRNA modifications are deposited in nascent pre-mRNA and are not required for splicing but do specify cytoplasmic turnover. Genes Dev. *31*, 990–1006. https://doi.org/10.1101/gad.301036.117.
15. He, P.C., Wei, J., Dou, X., Harada, B.T., Zhang, Z., Ge, R., Liu, C., Zhang, L.S., Yu, X., Wang, S., et al. (2023). Exon architecture controls mRNA m^{6}A suppression and gene expression. Science *379*, 677–682. https://doi.org/10.1126/science.abj9090.
16. Tang, P., Yang, J., Chen, Z., Du, C., Yang, Y., Zhao, H., Huang, L., Li, G., Liu, F., Dong, B., et al. (2024). Nuclear retention coupled with sequential polyadenylation dictates post-transcriptional m^{6}A modification in the nucleus. Mol. Cell *84*, 3758–3774.e10. https://doi.org/10.1016/j.molcel.2024.07.017.
17. Luo, Z., Ma, Q., Sun, S., Li, N., Wang, H., Ying, Z., and Ke, S. (2023). Exon-intron boundary inhibits m^{6}A deposition, enabling m^{6}A distribution hallmark, longer mRNA half-life and flexible protein coding. Nat. Commun. *14*, 4172. https://doi.org/10.1038/s41467-023-39897-1.
18. Uzonyi, A., Dierks, D., Nir, R., Kwon, O.S., Toth, U., Barbosa, I., Burel, C., Brandis, A., Rossmanith, W., Le Hir, H., et al. (2023). Exclusion of m^{6}A from splice-site proximal regions by the exon junction complex dictates m^{6}A topologies and mRNA stability. Mol. Cell *83*, 237–251.e7. https://doi.org/10.1016/j.molcel.2022.12.026.
19. Yang, X., Triboulet, R., Liu, Q., Sendinc, E., and Gregory, R.I. (2022). Exon junction complex shapes the m^{6}A epitranscriptome. Nat. Commun. *13*, 7904. https://doi.org/10.1038/s41467-022-35643-1.
20. Huang, H.L., Weng, H.Y., Zhou, K.R., Wu, T., Zhao, B.S., Sun, M.L., Chen, Z.H., Deng, X.L., Xiao, G., Auer, F., et al. (2019). Histone H3 trimethylation at lysine 36 guides m^{6}A RNA modification co-transcriptionally. Nature *567*, 414–419. https://doi.org/10.1038/s41586-019-1016-7.
21. Xu, W.Q., He, C.X., Kaye, E.G., Li, J.H., Mu, M.D., Nelson, G.M., Dong, L., Wang, J.H., Wu, F.Z., Shi, Y.G., et al. (2022). Dynamic control of chromatin-associated m^{6}A methylation regulates nascent RNA synthesis. Mol. Cell *82*, 1156–1168.e7. https://doi.org/10.1016/j.molcel.2022.02.006.
22. Lee, J.H., Wang, R.Y., Xiong, F., Krakowiak, J., Liao, Z., Nguyen, P.T., Moroz-Omori, E.V., Shao, J.F., Zhu, X.Y., Bolt, M.J., et al. (2021). Enhancer RNA m^{6}A methylation facilitates transcriptional condensate formation and gene activation. Mol. Cell *81*, 3368–3385.e9. https://doi.org/10.1016/j.molcel.2021.07.024.
23. Dou, X.Y., Xiao, Y., Shen, C., Wang, K., Wu, T., Liu, C., Li, Y.N., Yu, X.B., Liu, J., Dai, Q., et al. (2023). RBFOX2 recognizes N6-methyladenosine to suppress transcription and block myeloid leukaemia differentiation. Nat. Cell Biol. *25*, 1359–1368. https://doi.org/10.1038/s41556-023-01213-w.
24. Li, R., Zhao, H.Z., Huang, X.D., Zhang, J.L., Bai, R.H., Zhuang, L.S., Wen, S.J., Wu, S.J., Zhou, Q.B., Li, M., et al. (2023). Super-enhancer RNA m^{6}A promotes local chromatin accessibility and oncogene transcription in pancreatic ductal adenocarcinoma. Nat. Genet. *55*, 2224–2234. https://doi.org/10.1038/s41588-023-01568-8.
25. Seet, B.T., Dikic, I., Zhou, M.M., and Pawson, T. (2006). Reading protein modifications with interaction domains. Nat. Rev. Mol. Cell Biol. *7*, 473–483. https://doi.org/10.1038/nrm1960.
26. Sun, H.L., Zhu, A.C., Gao, Y., Terajima, H., Fei, Q., Liu, S., Zhang, L., Zhang, Z., Harada, B.T., He, Y.Y., et al. (2020). Stabilization of ERK-Phosphorylated METTL3 by USP5 Increases m^{6}A Methylation. Mol. Cell *80*, 633–647.e7. https://doi.org/10.1016/j.molcel.2020.10.026.
27. Zhang, C., Chen, L., Peng, D., Jiang, A., He, Y., Zeng, Y., Xie, C., Zhou, H., Luo, X., Liu, H., et al. (2020). METTL3 and N6-Methyladenosine Promote Homologous Recombination-Mediated Repair of DSBs by Modulating DNA-RNA Hybrid Accumulation. Mol. Cell *79*, 425–442.e7. https://doi.org/10.1016/j.molcel.2020.06.017.
28. Du, Y., Hou, G., Zhang, H., Dou, J., He, J., Guo, Y., Li, L., Chen, R., Wang, Y., Deng, R., et al. (2018). SUMOylation of the m6A-RNA methyltransferase METTL3 modulates its function. Nucleic Acids Res. *46*, 5195–5208. https://doi.org/10.1093/nar/gky156.
29. Liu, X., Wang, H., Zhao, X., Luo, Q., Wang, Q., Tan, K., Wang, Z., Jiang, J., Cui, J., Du, E., et al. (2021). Arginine methylation of METTL14 promotes RNA N^6-methyladenosine modification and endoderm differentiation of mouse embryonic stem cells. Nat. Commun. *12*, 3780. https://doi.org/10.1038/s41467-021-24035-6.
30. Li, Y.P., He, X.N., Lu, X., Gong, Z.C., Li, Q., Zhang, L., Yang, R.H., Wu, C.Y., Huang, J.L., Ding, J.C., et al. (2022). METTL3 acetylation impedes cancer metastasis via fine-tuning its nuclear and cytosolic functions. Nat. Commun. *13*, 6350. https://doi.org/10.1038/s41467-022-34209-5.
31. Liu, C., Yu, M., Wang, M.Y., Yang, S.Y., Fu, Y.A., Zhang, L., Zhu, C.Y., and Zhang, H.Q. (2024). PCAF-mediated acetylation of METTL3 impairs mRNA translation efficiency in response to oxidative stress. Sci. China Life Sci. *67*, 2157–2168. https://doi.org/10.1007/s11427-023-2535-x.
32. Kodama, Y., and Hu, C.D. (2010). An improved bimolecular fluorescence complementation assay with a high signal-to-noise ratio. BioTechniques *49*, 793–805. https://doi.org/10.2144/000113519.
33. Doench, J.G., Fusi, N., Sullender, M., Hegde, M., Vaimberg, E.W., Donovan, K.F., Smith, I., Tothova, Z., Wilen, C., Orchard, R., et al. (2016). Optimized sgRNA design to maximize activity and minimize off-target effects of CRISPR-Cas9. Nat. Biotechnol. *34*, 184–191. https://doi.org/10.1038/nbt.3437.
34. Watanabe, N., and Osada, H. (2016). Small molecules that target phosphorylation dependent protein-protein interaction. Bioorg. Med. Chem. *24*, 3246–3254. https://doi.org/10.1016/j.bmc.2016.03.023.

Please cite this article in press as: Huang et al., Spatial control of m^6A deposition on enhancer and promoter RNAs through co-acetylation of METTL3 and H3K27 on chromatin, Molecular Cell (2025), https://doi.org/10.1016/j.molcel.2025.02.016

35. Narita, T., Weinert, B.T., and Choudhary, C. (2019). Functions and mechanisms of non-histone protein acetylation. Nat. Rev. Mol. Cell Biol. *20*, 156–174. https://doi.org/10.1038/s41580-018-0081-3.

36. Molli, P.R., Li, D.Q., Murray, B.W., Rayala, S.K., and Kumar, R. (2009). PAK signaling in oncogenesis. Oncogene *28*, 2545–2555. https://doi.org/10.1038/onc.2009.119.

37. Hatzi, K., Jiang, Y.W., Huang, C.X., Garrett-Bakelman, F., Gearhart, M.D., Giannopoulou, E.G., Zumbo, P., Kirouac, K., Bhaskara, S., Polo, J.M., et al. (2013). A Hybrid Mechanism of Action for BCL6 in B Cells Defined by Formation of Functionally Distinct Complexes at Enhancers and Promoters. Cell Rep. *4*, 578–588. https://doi.org/10.1016/j.celrep.2013.06.016.

38. Ferrie, J.J., Karr, J.P., Graham, T.G.W., Dailey, G.M., Zhang, G.R., Tjian, R., and Darzacq, X. (2024). p300 is an obligate integrator of combinatorial transcription factor inputs. Mol. Cell *84*, 234–243.e4. https://doi.org/10.1016/j.molcel.2023.12.004.

39. Abu Bakar, Z.H., Bellier, J.P., Wan Ngah, W.Z.W., Yanagisawa, D., Mukaisho, K.I., and Tooyama, I. (2023). Optimization of 3D Immunofluorescence Analysis and Visualization Using IMARIS and MeshLab. Cells *12*, 218. https://doi.org/10.3390/cells12020218.

40. Sievers, F., Wilm, A., Dineen, D., Gibson, T.J., Karplus, K., Li, W.Z., Lopez, R., McWilliam, H., Remmert, M., Söding, J., et al. (2011). Fast, scalable generation of high-quality protein multiple sequence alignments using Clustal Omega. Mol. Syst. Biol. *7*, 539. https://doi.org/10.1038/msb.2011.75.

41. Kon, N., Churchill, M., Li, H., Mukherjee, S., Manfredi, J.J., and Gu, W. (2021). Robust p53 Stabilization Is Dispensable for Its Activation and Tumor Suppressor Function. Cancer Res. *81*, 935–944. https://doi.org/10.1158/0008-5472.Can-20-1804.

42. Kaya-Okur, H.S., Wu, S.J., Codomo, C.A., Pledger, E.S., Bryson, T.D., Henikoff, J.G., Ahmad, K., and Henikoff, S. (2019). CUT&Tag for efficient epigenomic profiling of small samples and single cells. Nat. Commun. *10*, 1930. https://doi.org/10.1038/s41467-019-09982-5.

43. Wang, C.W., Xu, H.D., Lin, S.F., Deng, W.K., Zhou, J.Q., Zhang, Y., Shi, Y., Peng, D., and Xue, Y. (2020). GPS 5.0: An Update on the Prediction of Kinase-specific Phosphorylation Sites in Proteins. Genomics Proteomics Bioinformatics *18*, 72–80. https://doi.org/10.1016/j.gpb.2020.01.001.

44. Kinoshita, E., Kinoshita-Kikuta, E., Takiyama, K., and Koike, T. (2006). Phosphate-binding tag, a new tool to visualize phosphorylated proteins. Mol. Cell. Proteomics *5*, 749–757. https://doi.org/10.1074/mcp.T500024-MCP200.

45. Zhu, M., Han, Y.L., Gu, T.N., Wang, R., Si, X.H., Kong, D.L., Zhao, P., Wang, X.J., Li, J.X., Zhai, X.Y., et al. (2024). Class I HDAC inhibitors enhance antitumor efficacy and persistence of CAR-T cells by activation of the Wnt pathway. Cell Rep. *43*, 114065. https://doi.org/10.1016/j.celrep.2024.114065.

46. Liu, C., Sun, H.X., Yi, Y.P., Shen, W.G., Li, K., Xiao, Y., Li, F., Li, Y.C., Hou, Y.K., Lu, B., et al. (2023). Absolute quantification of single-base m^6A methylation in the mammalian transcriptome using GLORI. Nat. Biotechnol. *41*, 355–366. https://doi.org/10.1038/s41587-022-01487-9.

47. Louloupi, A., Ntini, E., Conrad, T., and Ørom, U.A.V. (2018). Transient N-6-Methyladenosine Transcriptome Sequencing Reveals a Regulatory Role of m6A in Splicing Efficiency. Cell Rep. *23*, 3429–3437. https://doi.org/10.1016/j.celrep.2018.05.077.

48. ENCODE Project Consortium (2012). An integrated encyclopedia of DNA elements in the human genome. Nature *489*, 57–74. https://doi.org/10.1038/nature11247.

49. Luo, Y.H., Hitz, B.C., Gabdank, I., Hilton, J.A., Kagda, M.S., Lam, B., Myers, Z., Sud, P., Jou, J., Lin, K., et al. (2020). New developments on the Encyclopedia of DNA Elements (ENCODE) data portal. Nucleic Acids Res. *48*, D882–D889. https://doi.org/10.1093/nar/gkz1062.

50. Sdelci, S., Rendeiro, A.F., Rathert, P., You, W.H., Lin, J.G., Ringler, A., Hofstätter, G., Moll, H.P., Gürtl, B., Farlik, M., et al. (2019). MTHFD1 interaction with BRD4 links folate metabolism to transcriptional regulation. Nat. Genet. *51*, 990–998. https://doi.org/10.1038/s41588-019-0413-z.

51. Schick, S., Rendeiro, A.F., Runggatscher, K., Ringler, A., Boidol, B., Hinkel, M., Májek, P., Vulliard, L., Penz, T., Parapatics, K., et al. (2019). Systematic characterization of BAF mutations provides insights into intracomplex synthetic lethalities in human cancers. Nat. Genet. *51*, 1399–1410. https://doi.org/10.1038/s41588-019-0477-9.

52. Xu, C., Kleinschmidt, H., Yang, J., Leith, E., Johnson, J., Tan, S., Mahony, S., and Bai, L. (2023). Systematic Dissection of Sequence Features Affecting the Binding Specificity of a Pioneer Factor Reveals Binding Synergy Between FOXA1 and AP-1. Mol. Cell *84*, 2838–2855.e10. https://doi.org/10.1101/2023.11.08.566246.

53. Karolchik, D., Hinrichs, A.S., Furey, T.S., Roskin, K.M., Sugnet, C.W., Haussler, D., and Kent, W.J. (2004). The UCSC Table Browser data retrieval tool. Nucleic Acids Res. *32*, D493–D496. https://doi.org/10.1093/nar/gkh103.

54. Collins, B.E., Greer, C.B., Coleman, B.C., and Sweatt, J.D. (2019). Histone H3 lysine K4 methylation and its role in learning and memory. Epigenetics Chromatin *12*, 7. https://doi.org/10.1186/s13072-018-0251-8.

55. Heintzman, N.D., Hon, G.C., Hawkins, R.D., Kheradpour, P., Stark, A., Harp, L.F., Ye, Z., Lee, L.K., Stuart, R.K., Ching, C.W., et al. (2009). Histone modifications at human enhancers reflect global cell-type-specific gene expression. Nature *459*, 108–112. https://doi.org/10.1038/nature07829.

56. Millán-Zambrano, G., Burton, A., Bannister, A.J., and Schneider, R. (2022). Histone post-translational modifications - cause and consequence of genome function. Nat. Rev. Genet. *23*, 563–580. https://doi.org/10.1038/s41576-022-00468-7.

57. Liu, J.D., Gao, M.W., He, J.P., Wu, K.X., Lin, S.Y., Jin, L.M., Chen, Y.P., Liu, H., Shi, J.J., Wang, X.W., et al. (2021). The RNA m^6A reader YTHDC1 silences retrotransposons and guards ES cell identity. Nature *591*, 322–326. https://doi.org/10.1038/s41586-021-03313-9.

58. Jiang, X.J., Stockwell, B.R., and Conrad, M. (2021). Ferroptosis: mechanisms, biology and role in disease. Nat. Rev. Mol. Cell Biol. *22*, 266–282. https://doi.org/10.1038/s41580-020-00324-8.

59. Li, Y., Lu, Q., Xie, C., Yu, Y., and Zhang, A. (2022). Recent advances on development of p21-activated kinase 4 inhibitors as anti-tumor agents. Front. Pharmacol. *13*, 956220. https://doi.org/10.3389/fphar.2022.956220.

60. Guo, J.P., Xu, B.F., Han, Q., Zhou, H.X., Xia, Y., Gong, C.W., Dai, X.F., Li, Z.Y., and Wu, G. (2018). Ferroptosis: A Novel Anti-tumor Action for Cisplatin. Cancer Res. Treat. *50*, 445–460. https://doi.org/10.4143/crt.2016.572.

61. Rottenberg, S., Disler, C., and Perego, P. (2021). The rediscovery of platinum-based cancer therapy. Nat. Rev. Cancer *21*, 37–50. https://doi.org/10.1038/s41568-020-00308-y.

62. Yu, F., Wei, J., Cui, X., Yu, C., Ni, W., Bungert, J., Wu, L., He, C., and Qian, Z. (2021). Post-translational modification of RNA m^6A demethylase ALKBH5 regulates ROS-induced DNA damage response. Nucleic Acids Res. *49*, 5779–5797. https://doi.org/10.1093/nar/gkab415.

63. Zhou, J., Wan, J., Gao, X., Zhang, X., Jaffrey, S.R., and Qian, S.B. (2015). Dynamic m(6)A mRNA methylation directs translational control of heat shock response. Nature *526*, 591–594. https://doi.org/10.1038/nature15377.

64. Dong, F., Qin, X., Wang, B., Li, Q., Hu, J., Cheng, X., Guo, D., Cheng, F., Fang, C., Tan, Y., et al. (2021). ALKBH5 Facilitates Hypoxia-Induced Paraspeckle Assembly and IL8 Secretion to Generate an Immunosuppressive Tumor Microenvironment. Cancer Res. *81*, 5876–5888. https://doi.org/10.1158/0008-5472.CAN-21-1456.

65. Zhou, J., Wan, J., Shu, X.E., Mao, Y., Liu, X.M., Yuan, X., Zhang, X., Hess, M.E., Brüning, J.C., and Qian, S.B. (2018). N^6-Methyladenosine Guides mRNA Alternative Translation during Integrated Stress Response. Mol. Cell *69*, 636–647.e7. https://doi.org/10.1016/j.molcel.2018.01.019.

Please cite this article in press as: Huang et al., Spatial control of m^6A deposition on enhancer and promoter RNAs through co-acetylation of METTL3 and H3K27 on chromatin, Molecular Cell (2025), https://doi.org/10.1016/j.molcel.2025.02.016

66. Cun, Y., Guo, W., Ma, B., Okuno, Y., and Wang, J. (2024). Decoding the specificity of m^6A RNA methylation and its implication in cancer therapy. Mol. Ther. *32*, 2461–2469. https://doi.org/10.1016/j.ymthe.2024.05.035.

67. Dou, X.Y., Huang, L.L., Xiao, Y., Liu, C., Li, Y.N., Zhang, X.N., Yu, L.S., Zhao, R., Yang, L., Chen, C., et al. (2023). METTL14 is a chromatin regulator independent of its RNA N6-methyladenosine methyltransferase activity. Protein Cell *14*, 683–697. https://doi.org/10.1093/procel/pwad009.

68. Mu, M., Li, X., Dong, L., Wang, J., Cai, Q., Hu, Y., Wang, D., Zhao, P., Zhang, L., Zhang, D., et al. (2023). METTL14 regulates chromatin bivalent domains in mouse embryonic stem cells. Cell Rep. *42*, 113116. https://doi.org/10.1016/j.celrep.2023.113116.

69. Barbieri, I., Tzelepis, K., Pandolfini, L., Shi, J.W., Millán-Zambrano, G., Robson, S.C., Aspris, D., Migliori, V., Bannister, A.J., Han, N., et al. (2017). Promoter-bound METTL3 maintains myeloid leukaemia by m^6A-dependent translation control. Nature *552*, 126–131. https://doi.org/10.1038/nature24678.

70. Liu, P., Li, F., Lin, J., Fukumoto, T., Nacarelli, T., Hao, X., Kossenkov, A.V., Simon, M.C., and Zhang, R. (2021). m^6A-independent genome-wide METTL3 and METTL14 redistribution drives the senescence-associated secretory phenotype. Nat. Cell Biol. *23*, 355–365. https://doi.org/10.1038/s41556-021-00656-3.

71. Love, M.I., Huber, W., and Anders, S. (2014). Moderated estimation of fold change and dispersion for RNA-seq data with DESeq2. Genome Biol. *15*, 550. https://doi.org/10.1186/s13059-014-0550-8.

72. Martin, M. (2011). Cutadapt removes adapter sequences from high-throughput sequencing reads. EMBnet J. *17*, 10–12. https://doi.org/10.14806/EJ.17.1.200.

73. Dobin, A., Davis, C.A., Schlesinger, F., Drenkow, J., Zaleski, C., Jha, S., Batut, P., Chaisson, M., and Gingeras, T.R. (2013). STAR: ultrafast universal RNA-seq aligner. Bioinformatics *29*, 15–21. https://doi.org/10.1093/bioinformatics/bts635.

74. Tarasov, A., Vilella, A.J., Cuppen, E., Nijman, I.J., and Prins, P. (2015). Sambamba: fast processing of NGS alignment formats. Bioinformatics *31*, 2032–2034. https://doi.org/10.1093/bioinformatics/btv098.

75. Feng, J.X., Liu, T., Qin, B., Zhang, Y., and Liu, X.S. (2012). Identifying ChIP-seq enrichment using MACS. Nat. Protoc. *7*, 1728–1740. https://doi.org/10.1038/nprot.2012.101.

76. Quinlan, A.R., and Hall, I.M. (2010). BEDTools: a flexible suite of utilities for comparing genomic features. Bioinformatics *26*, 841–842. https://doi.org/10.1093/bioinformatics/btq033.

77. Wu, T.Z., Hu, E.Q., Xu, S.B., Chen, M.J., Guo, P.F., Dai, Z.H., Feng, T.Z., Zhou, L., Tang, W.L., Zhan, L., et al. (2021). clusterProfiler 4.0: A universal enrichment tool for interpreting omics data. Innovation (Camb) *2*, 100141. https://doi.org/10.1016/j.xinn.2021.100141.

78. Subramanian, A., Tamayo, P., Mootha, V.K., Mukherjee, S., Ebert, B.L., Gillette, M.A., Paulovich, A., Pomeroy, S.L., Golub, T.R., Lander, E.S., et al. (2005). Gene set enrichment analysis: A knowledge-based approach for interpreting genome-wide expression profiles. Proc. Natl. Acad. Sci. USA *102*, 15545–15550. https://doi.org/10.1073/pnas.0506580102.

79. Liberzon, A., Subramanian, A., Pinchback, R., Thorvaldsdóttir, H., Tamayo, P., and Mesirov, J.P. (2011). Molecular signatures database (MSigDB) 3.0. Bioinformatics *27*, 1739–1740. https://doi.org/10.1093/bioinformatics/btr260.

80. Ramírez, F., Ryan, D.P., Grüning, B., Bhardwaj, V., Kilpert, F., Richter, A.S., Heyne, S., Dündar, F., and Manke, T. (2016). deepTools2: a next generation web server for deep-sequencing data analysis. Nucleic Acids Res. *44*, W160–W165. https://doi.org/10.1093/nar/gkw257.

81. Langmead, B., and Salzberg, S.L. (2012). Fast gapped-read alignment with Bowtie 2. Nat. Methods *9*, 357–359. https://doi.org/10.1038/Nmeth.1923.

82. Li, W., Xu, H., Xiao, T., Cong, L., Love, M.I., Zhang, F., Irizarry, R.A., Liu, J.S., Brown, M., and Liu, X.S. (2014). MAGeCK enables robust identification of essential genes from genome-scale CRISPR/Cas9 knockout screens. Genome Biol. *15*, 554. https://doi.org/10.1186/s13059-014-0554-4.

83. Liu, Y.F., Han, R., Zhou, L.T., Luo, M.J., Zeng, L.D., Zhao, X.C., Ma, Y.K., Zhou, Z.L., and Sun, L. (2021). Comparative performance of the GenoLab M and NovaSeq 6000 sequencing platforms for transcriptome and LncRNA analysis. BMC Genomics *22*, 829. https://doi.org/10.1186/s12864-022-08307-z.

Please cite this article in press as: Huang et al., Spatial control of m^{6}A deposition on enhancer and promoter RNAs through co-acetylation of METTL3 and H3K27 on chromatin, Molecular Cell (2025), https://doi.org/10.1016/j.molcel.2025.02.016

STAR★METHODS

KEY RESOURCES TABLE

REAGENT or RESOURCE	SOURCE	IDENTIFIER
Antibodies		
HA-Tag (C29F4) Rabbit mAb	Cell Signaling	Cat# 3724 (also 3724S); RRID: AB_1549585
Myc-tag (9B11) Mouse mAb	Cell Signaling	Cat# 2276(also 2276S); RRID: AB_331783
P300 (D8Z4E) Rabbit mAb	Cell Signaling	Cat# 86377; RRID: AB_2800077
Beta-Tubulin Antibody	Cell Signaling	Cat# 2146 (also 2146S); RRID: AB_2210545
anti-Lamin B1	Cell Signaling	Cat# 13435 (also 13435S); RRID: AB_2737428
Histone H3 (D1H2) XP Rabbit mAb	Cell Signaling	Cat# 4499 (also 4499S, 4499P, 4499L); RRID: AB_10544537
Anti-mouse IgG, HRP-linked Antibody	Cell Signaling	Cat# 7076 (also 7076S, 7076V, 7076P2); RRID: AB_330924
FLAG (M2) Mouse mAb	Sigma-Aldrich	Cat# F1804; RRID: AB_262044
Monoclonal Anti-p300/CBP antibody produced in mouse	Sigma-Aldrich	Cat# P2859; RRID: AB_260994
Anti-METTL14 antibody produced in rabbit	Sigma-Aldrich	Cat# HPA038002; RRID: AB_10672401
METTL3 (EPR18810) Rabbit mAb	Abcam	Cat# ab195352; RRID: AB_2721254
Histone H3 (mono methyl K4) antibody	Abcam	Cat# ab8895; RRID: AB_306847
Histone H3 (acetyl K27) antibody	Abcam	Cat# ab4729; RRID: AB_2118291
Alexa Fluor® 488 linked anti-H3K27ac	Abcam	Cat# ab245911; RRID: AB_3096035
Alexa Fluor® 647 Rabbit monoclonal [EPR18810] to METTL3	Abcam	Cat# ab217109
Anti-Acetyllysine Mouse mAb	PTM BIO	Cat# PTM-101; RRID: AB_2940830
Anti-H3K4me3	ABclonal	Cat# A22146; RRID: AB_3066542
PAK2 Rabbit mAb	ABclonal	Cat# A4553; RRID: AB_2863294
GAPDH Rabbit mAb	ABclonal	Cat# A19056; RRID: AB_2862549
SNRNP70 Polyclonal Antibody	ABclonal	Cat# A14786; RRID: AB_2761662
Mouse TrueBlot ULTRA: Anti-Mouse Ig HRP	Rockland	Cat# 18-8817-33; RRID: AB_2610851
Rabbit TrueBlot: Anti-Rabbit IgG HRP	Rockland	Cat# 18-8816-33; RRID: AB_2610848
Goat anti-rabbit IgG (H+L), HRP conjugate	Proteintech	Cat# SA00001-2; RRID: AB_2722564
Mouse IgG (H+L) (Alexa Fluor™ Plus 647 linked)	Thermo Fisher Scientific	Cat# A32728; RRID: AB_2633277
Anti-Rabbit IgG (H+L) (Alexa Fluor™ Plus 488 linked)	Thermo Fisher Scientific	Cat# A32731; RRID: AB_2633280
Rabbit IgG (H+L) (Alexa Fluor™ Plus 405 linked)	Thermo Fisher Scientific	Cat# A48254; RRID: AB_2890548
Goat Anti-Rabbit IgG (H+L)	ABclonal	Cat# AS070; RRID:AB_2769651
Goat Anti-Mouse IgG (H+L)	ABclonal	Cat# AS071; RRID:AB_2769650
METTL3 Polyclonal antibody	Proteintech	Cat# 15073-1-AP; RRID:AB_2142033
METTL3-K215ac antibody	HUABIO	Customized
Chemicals, peptides, and recombinant proteins		
High-glucose (4.5.g/L) DMEM medium	Corning	10-013-CVRC
Fetal bovine serum	Sigma-Aldrich	F0193-500 ML
Ham's F-12K (Kaighn's) medium	Gibco	21127030
Opti-MEM	Gibco	31985070
TSA (Trichostatin A)	Selleck Chemicals	S1045
Nicotinamide	Medchem Express	HY-B0150
RSL3	Targetmol	T3646
ML162	Targetmol	T8970
Cisplatin	Targetmol	T1564
Ferrostatin-1	Targetmol	T6500

(*Continued on next page*)

Please cite this article in press as: Huang et al., Spatial control of m^{6}A deposition on enhancer and promoter RNAs through co-acetylation of METTL3 and H3K27 on chromatin, Molecular Cell (2025), https://doi.org/10.1016/j.molcel.2025.02.016

Continued

REAGENT or RESOURCE	SOURCE	IDENTIFIER
FRAX486	Targetmol	T6840
Liperfluo	DOJINDO	L248
PI	KeyGEN BioTECH	KGA1813-10
LentiFit	HANBIO	HB-LLF-1000
PEG6000	Sigma-Aldrich	81260
PEG20000	Sigma-Aldrich	81300
Polybrene	Santa Cruz	Sc-134220
Puromycin	Sigma-Aldrich	540411
doxycycline	Targetmol	T1687
RIPA Buffer (10 ×)	Cell Signaling	9806S
PMSF	Beyotime	ST506
6 × SDS sample buffer	TransGen Biotech	DL101-02
Tris-HCl pH=7.5	Thermo Fisher Scientific	15567027
IGEPAL CA-630	Sigma-Aldrich	I8896-50 ML
NaCl	Sigma-Aldrich	S5150-1 L
Glycerol	Sigma-Aldrich	G5516-100 ML
0.5 M EDTA, PH 8.0	Thermo Fisher Scientific	AM9261
Protease inhibitor cocktail	Medchem Express	HY-K0010
Phosphatase Inhibitor Cocktail II	Medchem Express	HY-K0022
Phos-tag (TM) Acrylamide AAL-107	Wako Diagnostics	300-93523
Protein A/G Magnetic Beads	Vazyme	PB101-02
Sucrose	Biofroxx	1245GR500
Tris-HCl pH=8.0	Invitrogen	AM9855G
DTT	Sigma-Aldrich	43816-10 ML
HEPES	Gibco	15630080
$MgCl_2$	Invitrogen	AM9530G
UREA	Sigma-Aldrich	51457
$CaCl_2$	Sigma-Aldrich	21115-100 ML
RNase A	Thermo Fisher Scientific	EN0531
TRI Reagent™	Invitrogen	AM9738
DMSO	Sigma-Aldrich	D2650-100 ML
Fragment buffer	New England Biolabs	E6150S
Glycogen	Thermo Fisher Scientific	AM9510
H_3BO_3	Sigma-Aldrich	B0394
$NaNO_2$	Sigma-Aldrich	31443
MES	Sigma-Aldrich	M3671
Glyoxal	Sigma-Aldrich	50649
Triethylamine	Sigma-Aldrich	471283
Sodium acetate solution	Thermo Fisher Scientific	R1181
Acetic acid	Sigma-Aldrich	695092-500 ML
Deionized formamide	Sigma-Aldrich	344206-M
VAHTS mRNA Capture Beads	Vazyme	N401-01
Trypsin	GIBCO	25200072
Coomassie Blue staining	Thermo Fisher Scientific	24617
Tritonx-100	Sigma-Aldrich	T9284-100 ML
DAPI	KeyGEN BioTECH	KGA1808-50
Blotting-Grade Blocker, nonfat dry milk	Bio-RAD	1706404
TURBO™ DNase I	Thermo Fisher Scientific	AM2238
AMPure XP beads	Beckman	A63881
PageRuler Prestained Protein Ladder	Thermo Fisher Scientific	26616

(*Continued on next page*)

Please cite this article in press as: Huang et al., Spatial control of m^6A deposition on enhancer and promoter RNAs through co-acetylation of METTL3 and H3K27 on chromatin, Molecular Cell (2025), https://doi.org/10.1016/j.molcel.2025.02.016

Continued

REAGENT or RESOURCE	SOURCE	IDENTIFIER
Multicolor Prestained Protein Ladder	Epizyme Biotech	WJ101
Critical commercial assays		
Pierce™ Rapid Gold BCA Protein Assay Kit	Thermo Fisher Scientific	A53226
Endo-free Plasmid Mini Kit II	Omega	D6950-02
Immunofluorescence Application Solutions Kit	Cell Signaling	12727S
VAHTS Universal V10 RNA-seq Library Prep Kit for MGI	Vazyme	NRM606-01
SMARTer Stranded Total RNA-Seq Kit v2	TAKARA	634413
Ribo-MagOff rRNA Depletion Kit	Vazyme	N420-01
2 × Universal SYBR Green Fast qPCR Mix	ABclonal	RK21203
ABScript III RT Master Mix for qPCR with gDNA Remover	ABclonal	RK20429
FastPure Cell/Tissue Total RNA Isolation Kit V2	Vazyme	RC112-01
Quick-DNA Midiprep Plus Kit	Zymo	D4075
Lipomaster 3000 Transfection Reagent	Vazyme	TL301-01
Mut Express MultiS Fast Mutagenesis Kit V2 (Vazyme)	Vazyme	C215-01
RNA Clean & Concentrator™-5 RNA	ZYMO RESEARCH	R1015
Hyperactive Universal CUT&Tag Assay Kit	Vazyme	TD904
Deposited data		
CRISPR-screening, GLORI-seq, chromosome-associated RNA-seq, and mRNA-seq	This study	GEO: GSE272469
Raw data	This study	Mendeley Data: http://www.doi.org/10.17632/gr43vkr4s6.1
ChIP-seq data with A549 cells of EP300	ENCODE Project Consortium[48]; Luo et al.[49]	ENCODE: ENCSR000BPW
ChIP-seq data with A549 cells of H3K27ac	ENCODE Project Consortium[48]; Luo et al.[49]	ENCODE: ENCSR783SNV
ChIP-seq data with A549 cells of H3K4me1	ENCODE Project Consortium[48]; Luo et al.[49]	ENCODE: ENCSR636PIN
ChIP-seq data with A549 cells of H3K4me2	ENCODE Project Consortium[48]; Luo et al.[49]	ENCODE: ENCSR410BCN
ChIP-seq data with A549 cells of H3K4me3	ENCODE Project Consortium[48]; Luo et al.[49]	ENCODE: ENCSR203XPU
ChIP-seq data with A549 cells of H3K36me3	Sdelci et al.[50]; Schick et al.[51]	GEO: GSE108387
ChIP-seq data with A549 cells of H3K9me3	Xu et al.[52]	GEO: GSE247412
MeRIP-seq input data of HepG2 cells	Dou et al.[23]	GEO: GSE205709
Experimental models: Cell lines		
HEK293T	Cellcook	CC4003
A549	Cellcook	CC0202
HeLa	Cellcook	CC1101
HepG2	Cellcook	CC0118
Oligonucleotides		
sgNC	This study	GCCTAGTCTCGGTAAGAGTG
sgEP300-1	This study	CTGTAATAAGTGGCATCACG
sgEP300-2	This study	GGTACGACTAGGTACAGGCG
sgCAMK2G	This study	TTTCTAGCAACGATCCACGG
sgPAK2	This study	GTGTGCTCAAAATCAGATGG
sgCDK13	This study	AGGTAACGGTGGTAATGTAG
sgCDK2	This study	AAGCAGAGAGATCTCTCGGA
shMETTL3-1	This study	GCCAAGGAACAATCCATTGTT
shMETTL3-2	This study	GCTGCACTTCAGACGAATT

(*Continued on next page*)

Please cite this article in press as: Huang et al., Spatial control of m^{6}A deposition on enhancer and promoter RNAs through co-acetylation of METTL3 and H3K27 on chromatin, Molecular Cell (2025), https://doi.org/10.1016/j.molcel.2025.02.016

Continued

REAGENT or RESOURCE	SOURCE	IDENTIFIER
shMETTL14-1	This study	CCATGTACTTACAAGCCGATA
shMETTL14-2	This study	GCTAATGTTGACATTGACTTA
SiCtrl	This study	TTCTCCGAACGTGTCACGT
sip300-1	This study	CAGACAAGTCTTGGCATGGTA
sip300-2	This study	CTAGAGACACCTTGTAGTA
siCBP-1	This study	AATCCACAGTACCGAGAAATG
siCBP-2	This study	TTGCAAGGAGCTTCCCAAG
q-PCR GAPDH-F	This study	CCTGACCTGCCGTCTAGAAA
q-PCR GAPDH-R	This study	CCCTGTTGCTGTAGCCAAAT
q-PCR SLC1A5-F	This study	GCTACTCCCGGACACCAGAC
q-PCR SLC1A5-R	This study	GGTCTGCAGGAGGCTAGGTT
q-PCR AKR1C2-F	This study	CTTTTCCACAGGTAAGAAACGGT
q-PCR AKR1C2-R	This study	CCAGGACAGGCATGAAGTGA
q-PCR AKR1C1-F	This study	TCTCAAACACTGTCATGGCCT
q-PCR AKR1C1-R	This study	CAACCCTCCTGGATGACTTGG
q-PCR PGD-F	This study	ATGGCCCAAGCTGACATCG
q-PCR PGD-R	This study	CCGTCTTGTGGTGTCCCTAT
q-PCR SLC5A6-F	This study	CGACCCCCTCTTCCTTTTCC
q-PCR SLC5A6-R	This study	GTCTGTGATCTGCAGCCAGT
q-PCR SLC7A11-F	This study	TCGCTGTGAAGGAAAAAGCAC
q-PCR SLC7A11-R	This study	GGTGGACACAACAGGCTTTC
Recombinant DNA		
P300	MiaoLingBio	P62911
PCDH-puro	MiaoLingBio	P14577
PCDH-RFP	MiaoLingBio	P17211
PCDNA 3.1	Addgene	128034
PLVX-TetOne-TRE3GS-MCS-EF1a-Neo	MiaoLingBio	P49160
PCDH-CMV-MCS-EF1-RFP	MiaoLingBio	P17211
mVenus N1	MiaoLingBio	P32438
PEnCMV-HDAC1 (human) -3 × FLAG-SV40-Neo	MiaoLingBio	P32870
PEnCMV-HDAC2 (human) -3 × FLAG-SV40-Neo	MiaoLingBio	P6907
PCMV-HDAC3 (human) -FLAG-SV40-Neo	MiaoLingBio	P38134
PCDNA3.1-3 × HA-HDAC4	MiaoLingBio	P4892
PCMV-HDAC5 (human) -FLAG-SV40-Neo	MiaoLingBio	P37515
PCDNA3.1-HDAC6-3 × HA	MiaoLingBio	P9653
PCDNA3.1-HDAC7-3 × HA	MiaoLingBio	P9871
PEnCMV-CREBBP (human)-HA-SV40-Neo	MiaoLingBio	P29740
PLKO.1-Puro	MiaoLingBio	P0258
pCMV-PAK2 (human) -3 × HA-Neo	MiaoLingBio	P54599
PLKO.1-EGFP	MiaoLingBio	P0255
pCMV-METTL3 (human) -Neo	MiaoLingBio	P49740
PCDNA 3.1 CMV-HDAC2-HA	Generated in this study	N/A
PCDNA 3.1 CMV-HDAC3-HA	Generated in this study	N/A
PCDNA 3.1 CMV-FLAG-METTL3	Generated in this study	N/A
PCDNA 3.1 CMV-FLAG-METTL3-K177R	Generated in this study	N/A
PCDNA 3.1 CMV-FLAG-METTL3-K211R	Generated in this study	N/A
PCDNA 3.1 CMV-FLAG-METTL3-K215R	Generated in this study	N/A
PCDNA 3.1 CMV-FLAG-METTL3-K327R	Generated in this study	N/A

(*Continued on next page*)

Please cite this article in press as: Huang et al., Spatial control of m^{6}A deposition on enhancer and promoter RNAs through co-acetylation of METTL3 and H3K27 on chromatin, Molecular Cell (2025), https://doi.org/10.1016/j.molcel.2025.02.016

Continued

REAGENT or RESOURCE	SOURCE	IDENTIFIER
PCDNA 3.1 CMV-FLAG-METTL3-K578R	Generated in this study	N/A
PCDNA 3.1 CMV-FLAG-METTL3-K177-215-578R	Generated in this study	N/A
PCDNA 3.1 CMV-FLAG-METTL3-K177-215-578Q	Generated in this study	N/A
PCDNA 3.1 CMV-FLAG-METTL3-1-350aa	Generated in this study	N/A
PCDNA 3.1 CMV-FLAG-METTL3-201-580aa	Generated in this study	N/A
PCDNA 3.1 CMV-FLAG-METTL3-351-580aa	Generated in this study	N/A
PCDNA 3.1 CMV-FLAG-METTL3-S243A	Generated in this study	N/A
PCDNA 3.1 CMV-FLAG-METTL3-S243D	Generated in this study	N/A
PCDNA 3.1 CMV-HA-PAK2	Generated in this study	N/A
PLKO.1-sh-METTL3-1-EGFP	Generated in this study	N/A
PLKO.1-sh-METTL3-2-EGFP	Generated in this study	N/A
PLKO.1-sh-METTL3-1-puro	Generated in this study	N/A
PLKO.1-sh-METTL3-2-puro	Generated in this study	N/A
PLKO.1-sh-METTL14-1-puro	Generated in this study	N/A
PLKO.1-sh-METTL14-2-puro	Generated in this study	N/A
PCDNA 3.1 CMV-FLAG-METTL3-K177-215-578R	Generated in this study	N/A
PLVX-TRE3G-METTL3-copGFP	Generated in this study	N/A
PLVX-TRE3G-METTL3-K177-215-578R-copGFP	Generated in this study	N/A
PMD2.G	Addgene	#12259
PsPAX2	Addgene	#12260
Human sgRNA library Brunello in lentiCRISPRv2	Addgene	#73179
lenti-CRISPRv2-puro	Addgene	#98290
Software and algorithms		
DESeq2 (v.1.42.1)	Love et al.[71]	http://www.bioconductor.org/packages/release/bioc/html/DESeq2.html
Cutadapt	Martin[72]	https://github.com/marcelm/cutadapt/
STAR (v.2.7.10b)	Dobin et al.[73]	https://github.com/alexdobin/STAR/releases/tag/2.7.10b
Imaris 10.0	Oxford Instruments	https://imaris.oxinst.com/products/imaris-for-cell-biologists
FlowJo 10.8.1	Treestar	https://www.flowjo.com
GLORI-tools	Liu et al.[46]	https://github.com/liucongcas/GLORI-tools.
sambamba (v.1.0.0)	Tarasov et al.[74]	http://www.open-bio.org/wiki/Sambamba
MACS2 (v.2.2.7.1)	Feng et al.[75]	http://liulab.dfci.harvard.edu/MACS/
bedtools (v.2.30.0)	Quinlan and Hall[76]	https://packages.guix.gnu.org/packages/bedtools/2.30.0/
clusterProfiler R package (v.4.10.1)	Wu et al.[77]	https://github.com/YuLab-SMU/clusterProfiler
MSigDB C2 gene sets and C5 gene sets	Subramanian et al.[78]; Liberzon et al.[79]	https://www.gsea-msigdb.org/gsea/msigdb
GraphPad Prism 10.2.3	www.graphpad.com	RRID: SCR_002798
deepTools (v.3.5.1)	Ramírez et al.[80]	https://deeptools.readthedocs.io/en/latest/
Clustal Omega 1.2.4	Sievers et al.[40]	http://www.clustal.org/
trim_galore (version 0.6.7)	https://github.com/FelixKrueger/TrimGalore	https://github.com/FelixKrueger/TrimGalore
bowtie2 (v.2.5.1)	Langmead and Salzberg[81]	https://github.com/BenLangmead/bowtie2/releases/tag/v2.5.1
MAGeCK	Li et al.[82]	https://sourceforge.net/p/mageck/wiki/Home/

Please cite this article in press as: Huang et al., Spatial control of m^{6}A deposition on enhancer and promoter RNAs through co-acetylation of METTL3 and H3K27 on chromatin, Molecular Cell (2025), https://doi.org/10.1016/j.molcel.2025.02.016

EXPERIMENTAL MODEL AND STUDY PARTICIPANT DETAILS

Cell culture

HEK293T, A549, HeLa, and HepG2 cells were purchased from Guangzhou Cellcook Biotechnology Co LTD (Guangzhou, China). HEK293T, A549, and HepG2 cells were cultured in high-glucose (4.5 g/L) DMEM medium (10-013-CVRC, Corning) containing 10% fetal bovine serum (F0193-500ML, Sigma). A549 cells were grown in Ham's F-12K (Kaighn's) medium (21127030, Gibco) with 10% fetal bovine serum (F0193-500ML, Sigma). All cell lines were cultured in a humidified incubator at 37 °C under an atmosphere containing 5% CO_2.

Antibodies and reagents

METTL3-K215ac antibody (1:1000) was customized from HUABIO, China. Anti-FLAG (1:1000, FM1804), p300/CBP (1:1000, P2859), METTL14 (1:1000, HPA038002) antibodies were purchased from Sigma, USA. Anti-Rabbit IgG (H+L) (Alexa Fluor™ Plus 488 linked, 1:500, A32731), Mouse IgG (H+L) (Alexa Fluor™ Plus 647 linked,1:500, A32728), and Rabbit IgG (H+L) (Alexa Fluor™ Plus 405 linked, 1:500, A48254) antibodies were purchased From Thermo Fisher Scientific, USA. Anti-HA-Tag (1:2000, 3724S), Myc-Tag (1:1000, 2276S), p300 (1:1000, 86377), β-tubulin (1:500, 2146S), LaminB1 (1:500, 13435), H3 (1:1000, 4499S), mouse IgG HRP-linked (1:5000, 7076S) antibodies were purchased from Cell Signaling Technology, USA. Anti-METTL3 (1:1000, ab195352), METTL3 (Alexa Fluor® 647 linked, 1:500, ab217109), H3K4me1 (1:1000, ab8895), H3K27ac (1:1000, ab4729), and H3K27ac (Alexa Fluor® 488 linked, 1:500, ab245911) antibodies were purchased from Abcam, UK. Anti-Kac (1:1000, PTM-101) antibody was purchased from PTM BIO, China. Anti-H3K4me3 (1:1000, A22146), PAK2 (1:500, A4553), GAPDH (1:10000, A19056), SNRNP70 (1:1000, A14786), Rabbit IgG(H+L) (AS070), and Mouse IgG (H+L) (AS071) antibodies were purchased from ABclonal, China. Anti-METTL3 (1:1000, 15073-1-AP) and Rabbit IgG (H+L) HRP-linked (1:5000, SA00001) antibodies were purchased from Proteintech Group, China.

TrueBlot* Ultra Anti-Mouse IgG HRP-linked (1:3000, 18-8817-33) and TrueBlot*Ultra Anti-Rabbit IgG HRP-linked (1:3000, 18-8816-33) antibodies were purchased from Rockland, USA. Deacetylase inhibitor TSA was purchased from Selleck. Deacetylase inhibitor NAM was purchased from MCE. RSL3, ML162, Cisplatin (CDDP), Ferrostatin-1, and PAK2 inhibitor FRAX486 were purchased from TargetMol, China. Liperfluo was purchased from DOJINDO, JPN. PI staining was purchased from keyGEN BioTECH, China.

METHOD DETAILS

Plasmids

The Human sgRNA library Brunello in lentiCRISPRv2 (#73179) was obtained from Addgene, USA. The BiFC reporters containing N terminal (I152L) and C terminal of VENUS were respectively subcloned into pLVX-TetOne-TRE3GS-MCS-EF1a-Neo (P49160, MiaoLingBio) to generate TETon-BIFC reporters. The cDNA plasmids of METTL3 (P49740), p300 (P62911), HDAC1 (P32870), HDAC2 (P6907), HDAC3 (P38134), HDAC4 (P4892), HDAC5 (P37515), HDAC6 (P9653), HDAC7 (P9871), CREBBP (P29740), and PAK2 (P54599) were purchased from MiaoLingBio, China. We used pCDH-RFP or PCDNA3.1, as the carrier vector for these cDNAs. These genes were integrated into the destination vector using Gateway cloning. All mutants were generated using the Mut Express MultiS Fast Mutagenesis Kit V2 (Vazyme Biotech, China) and were integrated into the destination vector.

Transfection and Virus Production

For transient transfection, cells were transfected by Lipomaster 3000 Transfection Reagent (TL301-01, Vazyme Biotech, China) according to the manufacturer's instructions. Briefly, cells were seeded 24 hours before transfection, and the plasmids and Lipofectamine reagent were combined in Opti-MEM media. After 6 h, the media was replaced with regular media without antibiotics.

For lentivirus production, lentiviral constructs were co-transfected with the psPAX2 packaging plasmid and the pMD2.G VSV-G envelope-expressing plasmid into HEK293T cells through LentiFit (HB-LLF-1000, HANBIO, China) according to the manufacturer's instructions. The viruses were collected for 48 h, concentrated by the PEG Virus Precipitation Solution, and stored at -80 °C.

CRISPR-Cas9-mediated gene knockout

We used CRISPR-Cas9 technology to knock out EP300, PAK2, CDK2, CDK13, and CAMK2G. Each sgRNA was cloned into the empty backbone of lenti-CRISPRv2-puro. Then, lenti-CRISPRv2-puro-based viruses were produced as described in the 'Transfection and Virus Production' section. Subsequently, A549, HeLa, and other cells were infected with the virus and 1 μg/ml polybrene for 24 h. Finally, cells were selected with puromycin (6 μg/ml; Sigma, USA) for 3 days. The sgRNA sequences are displayed in the key resources table.

shRNA-mediated RNA interference

The shRNAs of METTL3 and METTL14 were cloned into the empty backbone of lentivirus-based pLKO.1-puro or pLKO.1-EGFP. Then, PLKO.1-based viruses were produced according to as described in the 'Transfection and Virus Production' section. Subsequently, A549, HeLa, and other cells were infected with the virus and 1 μg/ml polybrene for 24 h. Finally, cells were selected with puromycin (6 μg/ml; Sigma, USA) for 3 days. The shRNA sequences are displayed in the key resources table.

Please cite this article in press as: Huang et al., Spatial control of m^{6}A deposition on enhancer and promoter RNAs through co-acetylation of METTL3 and H3K27 on chromatin, Molecular Cell (2025), https://doi.org/10.1016/j.molcel.2025.02.016

siRNA-mediated RNA interference

All siRNAs were produced by GenePharma and transfected using RNAFit Transfection Reagent (HB-RF-1000, HANBIO, China) according to the manufacturer's protocol. The siRNA sequences are displayed in the key resources table.

Genome-wide CRISPR/Cas9 screening

CRISPR screen in A549 cells with stably expressed TETon-BIFC reporter. A549 cells with stably expressed TETon-BIFC reporter (1.2×10^8 cells) were transduced with a genome-wide gRNA library Brunello in lentiCRISPRv2 (73179, Addgene, USA) at a multiplicity of infection (MOI) of 0.3. Cells with stably transduced genome-wide gRNA library were selected with 5 μg/ml puromycin, and 4.5×10^7 cells were passaged every 48-72 hours at a density of 5×10^6 cells per 15 cm dish in Ham's F-12K (Kaighn's) medium for the duration of the screen. At 5 days post puromycin selection, cells were treated with doxycycline (1 μg/mL) for 48 hours. Next, 1.5×10^8 cells were sorted by flow cytometry sorting and collected 5% in high-VENUS-signal cells and low-VENUS-signal cells. Genomic DNA was isolated using a Quick-gDNA MidiPrep (Zymo Research, USA). sgRNA after PCR amplification was sent to the GENEWIZ (Suzhou, China) to be sequenced on Illumina NovaSeq 6000.

sgRNA sequencing data analysis

Raw reads were trimmed using Cutadapt to remove the constant flanking sequences of sgRNA sequences.[72] Read counts of the sgRNAs were calculated by the count command of MAGeCK.[82] The sgRNAs with MAGeCK normalized read counts of high-VENUS-signal or low-VENUS-signal samples < 200 were removed for further analysis. Then, the test command of MAGeCK was used to calculate the p values for the comparison between two samples of sgRNAs. The Genes with p value < 0.01 and fold change (high-VENUS-signal/low-VENUS-signal) > 1.5 were identified as the gene enriched in high-VENUS-signal populations. Meanwhile, genes with p value < 0.01 and fold change (low-VENUS-signal/high-VENUS-signal) > 1.5 were identified as genes enriched in low-VENUS-signal populations.

Western blotting and co-immunoprecipitation (co-IP)

Whole-cell extracts were generated by direct lysis with water-diluted RIPA lysis buffer (9806S, Cell Signaling Technology, USA), adding 1 mM phenylmethylsulphonyl fluoride (PMSF; ST506, Beyotime Biotech, China) immediately before use. Lysates were sonicated, and then centrifuged at 12,000 g for 15 min at 4 °C. Samples were boiled by adding 6 × SDS sample buffer for 10 min at 100 °C and resolved using SDS-PAGE. For co-immunoprecipitation, cells were lysed by IP lysis buffer (25 mM Tris-HCl pH = 7.5, 0.1% IGEPAL CA-630, 250 mM NaCl, 5% glycerol, 5 mM EDTA) with 1% protease inhibitor cocktail (HY-K0010, MCE, USA), 1% Phosphatase Inhibitor cocktail II (HY-K0022, MCE, USA), 1 mM PMSF, 1 μM TSA, and 5 mM NAM. Then, cell lysates were sonicated and centrifuged at 12,000 g for 15 min at 4 °C. Immunoprecipitation was carried out by incubating the appropriate antibody with cell lysate overnight at 4 °C, followed by incubating Protein A/G Magnetic Beads (PB101-02, Vazyme Biotech, China) for 2 hours at 4 °C. Immunoprecipitates were washed three times with cold IP lysis buffer, eluted with 2 × SDS loading buffer by boiling for 10 min, and resolved using SDS-PAGE.

Phosphate-affinity gel electrophoresis

Phosphate-affinity gel electrophoresis was performed in gels containing 50 mM $MnCl_2$ and 50 mM acrylamide-pendant Phosphate-Tag ligand according to the manufacturer's protocols (AAL-107, Wako Chemicals, JPN). The cell lysates were purified to remove the lysis buffer containing EDTA by Ultrafiltration Spin Columns (FUF051-5pcs, Beyotime, China) and dissolved in 1 × SDS sample buffer before Phosphate-affinity gel electrophoresis. Then, proteins were resolved using Phosphate-affinity gel. Before transmembrane, Phosphate-affinity gel was washed three times by trans buffer containing 5 mmol/L EDTA.

Cell fractionation

A549 and HEK293T cells were fractionated following the previously published procedure.[2] Briefly, 1×10^7 cells were collected, washed with 1 ml cold PBS buffer containing 1 mM EDTA, and centrifuged at 500 g and room temperature for 5 min. Added 200 uL ice-cold cytoplasmic lysis buffer (10 mM Tris-HCl pH = 7.5, 0.1% IGEPAL®CA-630, 150 mM NaCl) to the cell pellet and incubated on ice for 5 min, then added 2.5 volumes of chilled sucrose cushion (24% RNAse-free sucrose in cytoplasmic lysis buffer). Subsequently, centrifuge at 15,000g and 4 °C for 10 min. The supernatant was collected as the cytoplasmic fraction. Added 100 μL of pre-chilled glycerol buffer (20 mM Tris-HCl pH = 7.9, 75 mM NaCl, 0.5 mM EDTA, 0.85 mM DTT, 0.125 mM PMSF, 50% glycerol) to resuspend the nuclei pellet, then added an equal volume of cold nuclei lysis buffer (10 mM HEPES pH = 7.6, 1 mM DTT, 7.5 mM $MgCl_2$, 0.2 mM EDTA, 0.3 M NaCl, 1 M UREA, 1% IGEPAL®CA-630) and vigorously vortexed. The mixtures of nuclei pellets were incubated on ice for 2 min, then centrifuged at 4 °C with 15,000 g for 2 min. The supernatant is soluble nucleoplasm, and the pellet is chromatin fraction.

Chromatin-associated protein co-immunoprecipitation

The chromatin pellets were first obtained as described in the 'Cell fractionation' section to analyze the protein interaction of METTL3 and METTL3 acetylation on chromatin. The chromatin pellets were lysed by 200 μL chromatin lysis buffer (25 mM Tris-HCl pH = 7.5, 0.1% IGEPAL CA-630, 250 mM NaCl, 5% glycerol, 5 mM $MgCl_2$) with 1% protease inhibitor cocktail, 1% Phosphatase Inhibitor

Please cite this article in press as: Huang et al., Spatial control of m^{6}A deposition on enhancer and promoter RNAs through co-acetylation of METTL3 and H3K27 on chromatin, Molecular Cell (2025), https://doi.org/10.1016/j.molcel.2025.02.016

Cocktail II, 1mM PMSF, 1 μM TSA, and 5 mM NAM. Then, lysates of chromatin pellets were sonicated at 4 °C. Subsequently, TURBO™ DNase I (AM2238, Thermo Fisher Scientific, USA) and RNase A (EN0531, Thermo Fisher Scientific, USA) were respectively added to lysates with 50 units/ml and 30 μg/ml and incubated at 30 °C for 30 min. Next, lysates were diluted to 1 mL by using IP lysis buffer (25 mM Tris-HCl pH = 7.5, 0.1% IGEPAL CA-630, 250 mM NaCl, 5% glycerol, 5 mM EDTA) with 1% protease inhibitor cocktail, 1% Phosphatase Inhibitor Cocktail II, and 1 mM PMSF. Finally, immunoprecipitation was carried out by incubating the appropriate antibody with cell lysate overnight at 4 °C, followed by incubating Protein A/G Magnetic Beads for 2 hours at 4 °C. Immunoprecipitates were washed three times with cold IP lysis buffer, eluted with 2 × SDS loading buffer by boiling for 10 min, and resolved using SDS-PAGE.

RNA extraction and quantitative real-time PCR

The total RNA was extracted from cells using FastPure Cell/Tissue Total RNA Isolation Kit V2 (RC112-01, Vazyme Biotech, China). The RNA concentration was measured using a Nanodropone spectrophotometer (Thermo Fisher Scientific, USA). Total RNA was reverse transcribed using ABScript III RT Master Mix for qPCR with gDNA Remover kit for qPCR (RK20429-100T, ABclonal, China) and diluted 5 - 10 folds. cDNA amplification was performed using 2 × Universal SYBR Green Fast qPCR Mix (RK21203, ABclonal, China) with the LightCycle480 II PCR System (Roche, Switzerland) according to the manufacturer's protocol. The GAPDH was used as the internal control, and each sample was analyzed in triplicate. The results were analyzed using the $2^{-\Delta\Delta CT}$ method, and gene expression was reported relative to that of the internal control. The primer sequences for quantitative real-time PCR are displayed in the key resources table.

Chromatin-associated RNA (caRNA) extraction

To isolate the caRNA, the chromatin pellet was first obtained as described in the 'Cell fractionation' section. Then, the chromatin pellet was dissolved in 1 mL of TRI Reagent™ (AM9738, Invitrogen, USA) and heated at 50 °C with shaking at 1,000 rpm for 20 minutes until it completely dissolved. Finally, caRNAs were extracted according to the manufacturer's instructions for TRI Reagent™.

GLORI-seq of chromatin-associated RNAs

First, genomic DNA is removed from caRNAs by using DNase I (EN401, Vazyme). Subsequently, non-ribosomal caRNAs were further enriched by using the Ribo-MagOff rRNA Depletion Kit (N420-01, Vazyme Biotech, China). Then, GLORI was carried out according to previously published.[46] Briefly, caRNAs were fragmented at 94 °C for 30 s. Then, guanosine of fragmented caRNAs was protected in a protection buffer (1.32 M glyoxal, 50% DMSO) at 50 °C for 30 min. Subsequently, add 10 μl saturated H_3BO_3 solution and incubate at 50 °C for 30min. Next, add deamination buffer (750 mM $NaNO_2$, 40 mM MES buffer, and 2.08 M glyoxal) and incubate at 16 °C for 8 h to deaminize adenine. Finally, add deprotection buffer (0.25 M TEAA and 25% deionized formamide) and incubate at 95 °C for 10 minutes.

For library construction, SMARTer Stranded Total RNA-Seq Kits v2 Pico Input Mammalian (Takara, 634413) was used according to the manufacturer's protocols with some modified steps. In brief, about 50 ng GLORI-treated RNA was used for first-strand cDNA synthesis, and Illumina adapters and indexes were added to first-stranded cDNA. The PCR1 products were purified twice by using 0.8 × AMPure beads, then skipped the removal of the Ribosomal cDNA step and eluting cDNA with 20μL RNase-free H_2O. The purified cDNA was amplified by 9 to 11 cycles of PCR2, and followed by purification using 1 × AMPure beads. Finally, the library size distribution was evaluated by Qsep100NGS. The library sequencing was performed at GeneMind Biosciences Company (Shenzhen, China) through the SURFSeq 5000 platform on PE100 mode.[83]

caRNA-seq and RNA-seq

For caRNAs-seq, caRNAs without rRNA and genomic DNA were used to construct a library using the SMARTer Stranded Total RNA-Seq Kit v2 (Takara) according to the manufacturer's protocols. After the quality control, Sequencing was performed at BGI Company (Shenzhen, China) through the MGISEQ-2000 platform on PE150 mode.

For RNA-seq, total RNA was captured mRNA by using VAHTS mRNA Capture Beads (N401, Vazyme). Then, library preparation was performed by using the VAHTS Universal V10 RNA-seq Library Prep Kit for MGI (NRM606-01, Vazyme). After the quality control, Sequencing was performed at BGI Company (Shenzhen, China) through the MGISEQ-2000 platform on PE150 mode.

CUT&Tag

CUT&Tag experiments were performed by Hyperactive Universal CUT&Tag Assay Kit (TD904, Vazyme Biotech, China). Briefly, A549 cells were incubated and bound with ConA Beads Pro. Then, we added 50 μl cold Antibody Buffer dilution with Anti-METTL3 (1:50, 15073-1-AP, Proteintech, China) or Anti-H3K27ac (1:100, ab4729, Abcam, UK) antibodies to incubate for 12 h at 4 °C. Next day, secondary antibodies (1:100, AS070, ABclonal, China) were added and incubated for 1 hour at room temperature. The unbound antibodies were removed by Dig-Wash buffer and the pA-Tn5 adaptor complex was prepared and added to the nuclei with gentle vertexing. Washed nuclei were resuspended in the Tagmentation buffer and STOP buffer was used to stop fragmentation. The DNA library was purified and amplified for sequencing with the SURFSeq 5000 platform of GeneMind Biosciences Company (Shenzhen, China) on PE100 mode.[83]

Please cite this article in press as: Huang et al., Spatial control of m^6A deposition on enhancer and promoter RNAs through co-acetylation of METTL3 and H3K27 on chromatin, Molecular Cell (2025), https://doi.org/10.1016/j.molcel.2025.02.016

Mass spectrometry

To identify acetylation and phosphorylation sites of chromatin-associated METTL3, HEK293T cells co-transfected with FLAG-METTL3 and Myc-p300 or HA-PAK2, and then chromatin-associated METTL3 precipitated from chromatin fraction of HEK293T cells. Then the precipitate was analyzed by Coomassie Blue staining. The protein band corresponding to METTL3 was excised and subjected to in-gel digestion with trypsin. Mass spectrometry analysis was performed at Wininnovate Bio Company (Shenzhen, China) through Easy nLC 1200 system (ThermoFisher, USA) with Q Exactive mass spectrometer (ThermoFisher, USA) fitted with a Nano Flex ion source. The MS/MS data were analyzed for protein identification and quantification using PEAKS Studio 8.5. The local false discovery rate at PSM was 1.0% after searching against the Uniprot database with a maximum of two missed cleavages.

Immunofluorescence staining and image analyses

The cells, after treatments, were fixed in 4% paraformaldehyde, permeabilized with 0.25% Triton X-100, and blocked with 3% BSA at room temperature for 1 h. Then, the samples were incubated with dilution primary antibodies overnight at 4°C followed by incubation with the appropriate Fluorescent secondary antibody. Finally, Nuclei were stained with 4',6-diamidino-2-phenylindole (DAPI; keyGEN BioTECH, China). Images were acquired with the Nikon N-SIM Microscope System by using the 3D-SIM module (Nikon, JPN) or confocal microscopy (ZEISS, Germany).

3D-SIM data analysis was performed in Imaris software (Oxford Instruments UK). Briefly, the intermediate value of protein diameter is measured. Then, the spot model was used to reconstruct the proteins acquired from 3D-SIM. If the distance between different spots is less than the radius of the spot, the proteins represented by these spots were considered co-localized and were marked as yellow. The co-localization of p300-H3K27ac, p300-METTL3, METTL3-H3K27ac, HDAC1-H3K27ac, and HDAC1-METTL3 was calculated according to this definition.

Cell-death assays

We used PI staining to stain cells, followed by flow cytometry analysis to detect cell death. Briefly, cells were seeded in six-well plates of about 2.5×10^5 cells per well. The next day, the cells were treated with the indicated compounds. After treatment, all cells were collected and stained with 5 μg/ml PI staining (keyGEN BioTECH, China) at room temperature for 30 min. Cells were analyzed with flow cytometry (Beckman Coulter, USA). PI-positive cells were considered to be dead cells. At least 5,000 cells were detected in each group by flow cytometry. All experiments were repeated at least three times.

Determination of lipid peroxidation

Cells were seeded in six-well plates of about 2.5×10^5 cells per well. The next day, the cells were treated with the indicated compounds and then collected. The cells were stained with 2.5 μM Liperfluo at 37 °C for 30 min. Subsequently, samples were analyzed by flow cytometry (Beckman Coulter, USA). The fluorescence intensity in the FITC channel was detected.

Enzyme-linked immunosorbent assay (ELISA assay)

ELISA was performed by HUABIO company. Briefly, polystyrene plates was coated by 1 μg/mL of unmodified K215 (CEPAKKSRKHAASDV) and acetylated K215 (CEPAKKSRK(ac)HAASDV) peptide diluted in coating buffer for overnight at 4 °C, respectively. Following coating, the plates were blocked with 150 μL of 1% BSA at 37 °C for 1 hour. Subsequently, 1% BSA and different concentrations of METTL3-K215ac antibodies were added to detect peptides coated on polystyrene plates, respectively. After 1 h incubation at 37 °C, HRP-conjugated second antibodies were added and incubated to plates at 37 °C for 45 min. TMB substrate solution was then introduced to initiate the reaction, which was allowed to proceed at 37 °C for 5 min. The reaction was terminated by adding 1M sulfuric acid. Absorbance was measured at 450 nm using a microplate reader.

GLORI-seq analysis for chromatin-associated RNAs

The second ends of the paired-end reads, which correspond to the sense strand of the original RNA, were used in the analysis. Raw reads were treated with trim_galore (v.0.6.7) for adaptor trimming. Then, the reads were mapped to converted human reference genome (hg38) using STAR (v.2.7.10b) following the previous pipeline implemented in the provided GLORI-tools with default parameters.[46,73] m^6A level for each m^6A site was calculated as the fractions of unconverted reads in the total covered reads. The m^6A levels based on less than 15 total covered reads were removed from the analysis. Differential m^6A sites between R-METTL3-WT and R-METTL3-3KR were determined as those with absolute changes of the mean m^6A modification levels greater than 0.15.

Determination of promoter and enhancer regions

We defined the promoter and enhancer regions as previously described.[2] Promoter regions were determined as the regions located from 1 kb upstream to 100 bp downstream of the transcription start site (TSS). The enhancer regions were determined as the H3K27ac peaks within -50 kb to -5 kb upstream and 5 kb to 50 kb downstream of the TSS. We categorized the RNAs derived from enhancers as enhancer RNA (eRNA) and the RNA derived from promoters as promoter-associated RNA (paRNA). To ensure the exclusion of potential noise from nascent pre-mRNA, we further classified paRNAs into sense (paRNA [+], coding strand) and antisense paRNAs (paRNA [–], template strand) based on the transcript origins.

Please cite this article in press as: Huang et al., Spatial control of m^6A deposition on enhancer and promoter RNAs through co-acetylation of METTL3 and H3K27 on chromatin, Molecular Cell (2025), https://doi.org/10.1016/j.molcel.2025.02.016

mRNA-seq and caRNA-seq data analyses

Raw sequencing reads were preprocessed using trim_galore (version 0.6.7) for adapter trimming.[46] These reads were then aligned to the human reference genome (hg38) using STAR aligner (v.2.7.10b) with default parameters.[73] Only the uniquely mapped reads were used in the downstream analyses. Differentially expressed genes with 1.5-fold change and adjusted p value < 0.05 were determined using DESeq2 (v.1.42.1).[71] The transcript abundance for each eRNA and paRNA region was normalized by FPKM. BigWig files were produced using deepTools (v.3.5.1) bamCoverage with '–normalized using RPKM' parameters.[80]

ChIP-seq data and CUT&Tag data analyses

Raw ChIP-seq and CUT&Tag reads were preprocessed using trim_galore (version 0.6.7) for adapter trimming. These reads were then aligned to the human reference genome (hg38) using bowtie2 (v.2.5.1). PCR duplicates were removed using sambamba (v.1.0.0).[74,81] Only the uniquely mapped reads were used in the downstream analyses. The peaks were called using MACS2 (v.2.2.7.1).[75] Peaks from replicates were combined using bedtools (v.2.30.0) merge.[76] The METTL3 and H3K27ac peaks were quantified using FPKM calculation. The up-regulated and down-regulated METTL3 peaks between R-METTL3-WT and R-METTL3-3KR were determined as those with FPKMs of R-METTL3-3KR 1.5-fold higher or 1.5-fold lower than R-METTL3-WT respectively.

Gene ontology and pathway analyses

Gene ontology and pathway enrichment analyses were performed using the clusterProfiler R package (v.4.10.1).[77] Enrichment terms were determined using MSigDB C2 gene sets and C5 gene sets.[78,79]

TCGA data analysis

We obtained gene expression data pression data and corresponding clinical information from the TCGA database. Samples exhibiting METTL3 (or PAK2) expression levels above the mean were categorized into the METTL3-high (or PAK2-high) group, while those with expression levels below the mean were classified as the METTL3-low (or PAK2-low) group. Survival curves for these distinct patient groups were generated using the Kaplan-Meier method and compared using the log-rank test.

QUANTIFICATION AND STATISTICAL ANALYSIS

For quantitative real-time PCR and flow cytometry data, statistical analyses were conducted using the GraphPad Prism 10.2.3 software. The results are presented as the mean ± s.d. of three biologically independent experiments or samples. The p values were calculated using an unpaired Student's t-test or two-way ANOVA with Tukey's post hoc test. If p value less than 0.05 was considered significant. For survival analyses, Cox proportional hazards and log-rank tests were used.

For high-throughput data, statistical analyses were conducted using the R-studio. The statistical significances of differences were determined using two-sided Wilcoxon rank-sum test. Pearson correlation coefficients (PCCs) and p values were calculated to assess the correlations. For box plots, the center lines represent the median, the box limits show the upper and lower quartiles and the whiskers represent 1.5 × the interquartile range. For stacked bar plots, the p values were calculated by two-sided chi-squared test.